

Diagenesis Revealed by Fine Scale Features at Vera Rubin Ridge, Gale Crater, Mars

Kristen A. Bennett, Frances Rivera-Hernández, Connor Tinker, Briony Horgan, Deirdra M. Fey, Christopher Edwards, Lauren A. Edgar, Rachel Kronyak, Kenneth S. Edgett, Abigail Fraeman, et al.

▶ **To cite this version:**

Kristen A. Bennett, Frances Rivera-Hernández, Connor Tinker, Briony Horgan, Deirdra M. Fey, et al.. Diagenesis Revealed by Fine Scale Features at Vera Rubin Ridge, Gale Crater, Mars. Journal of Geophysical Research. Planets, 2021, 126, 10.1029/2019JE006311 . insu-03710146

HAL Id: insu-03710146
https://insu.hal.science/insu-03710146

Submitted on 6 Aug 2022

HAL is a multi-disciplinary open access archive for the deposit and dissemination of scientific research documents, whether they are published or not. The documents may come from teaching and research institutions in France or abroad, or from public or private research centers.

L'archive ouverte pluridisciplinaire **HAL**, est destinée au dépôt et à la diffusion de documents scientifiques de niveau recherche, publiés ou non, émanant des établissements d'enseignement et de recherche français ou étrangers, des laboratoires publics ou privés.

Copyright

Check for updates

JGR Planets

RESEARCH ARTICLE
10.1029/2019JE006311

Special Section:
Investigations of Vera Rubin Ridge, Gale Crater

Diagenesis Revealed by Fine-Scale Features at Vera Rubin Ridge, Gale Crater, Mars

Kristen A. Bennett[1], Frances Rivera-Hernández[2], Connor Tinker[3,4], Briony Horgan[3], Deirdra M. Fey[5], Christopher Edwards[6], Lauren A. Edgar[1], Rachel Kronyak[7], Kenneth S. Edgett[5], Abigail Fraeman[7], Linda C. Kah[8], Marie Henderson[3], Nathan Stein[9], Erwin Dehouck[10], and Amy J. Williams[11]

[1]Astrogeology Science Center, U.S. Geological Survey, Flagstaff, AZ, USA, [2]School of Earth and Atmospheric Sciences, Georgia Institute of Technology, Atlanta, GA, USA, [3]Earth, Atmospheric, and Planetary Sciences, Purdue University, West Lafayette, IN, USA, [4]Department of Geosciences, Stony Brook University, Stony Brook, NY, USA, [5]Malin Space Science Systems, San Diego, CA, USA, [6]Department of Astronomy and Planetary Science, Northern Arizona University, Flagstaff, AZ, USA, [7]Jet Propulsion Laboratory, California Institute of Technology, Pasadena, CA, USA, [8]Department of Earth and Planetary Sciences, University of Tennessee, TN, USA, [9]California Institute of Technology, Pasadena, CA, USA, [10]Université de Lyon, UCBL, ENSL, CNRS, LGL-TPE, Villeurbanne, France, [11]Department of Geological Sciences, University of Florida, Gainesville, FL, USA

Key Points:

- We investigate depositional and diagenetic features on Vera Rubin ridge using high-spatial resolution images
- Observations of submillimeter-to-centimeter scale features indicate extensive diagenesis occurred in this area
- Subtle deviations in grain size likely contributed to the distribution and variability of diagenesis

Supporting Information:

Supporting Information may be found in the online version of this article.

Correspondence to:

K. A. Bennett,
kbennett@usgs.gov

Citation:

Bennett, K. A., Rivera-Hernández, F., Tinker, C., Horgan, B., Fey, D. M., Edwards, C., et al. (2021). Diagenesis revealed by fine-scale features at Vera Rubin ridge, Gale crater, Mars. *Journal of Geophysical Research: Planets*, *126*, e2019JE006311. https://doi.org/10.1029/2019JE006311

Received 5 DEC 2019
Accepted 25 MAR 2021

© 2021. Jet Propulsion Laboratory, California Institute of Technology. Government sponsorship acknowledged. This article has been contributed to by US Government employees and their work is in the public domain in the USA.

Abstract Fine-scale (submillimeter to centimeter) depositional and diagenetic features encountered during the *Curiosity* rover's traverse in Gale crater provide a means to understand the geologic history of Vera Rubin ridge (VRR). VRR is a topographically high feature on the lower north slope of Aeolis Mons, a 5-km high stratified mound within Gale crater. We use high-spatial resolution images from the Mars Hand Lens Imager (MAHLI) as well as grain sizes estimated with the Gini index mean score technique that uses ChemCam Laser-Induced Breakdown Spectroscopy (LIBS) chemical data to constrain the postdepositional history of the strata exposed on this ridge. MAHLI images were used to examine the color, grain size, and style of lamination of the host rocks, as well as to explore the occurrence of nodules, diagenetic crystals, pits, and a variety of dark-gray iron-rich features. This survey revealed abundant and widespread diagenetic features within the rocks exposed on VRR and demonstrated that rock targets estimated to be coarser generally contain more diagenetic features than those estimated to have finer grains, which indicate that grain size may have influenced the degree and type of diagenesis. A subset of rocks within VRR are gray in color and exhibit the highest proportion of diagenetic features. We suggest that these targets experienced a different diagenetic history than the other rocks on VRR and hypothesize that redistribution and recrystallization of iron within specific intervals may have resulted in both the gray color and the abundance of dark-gray iron-rich diagenetic features.

Plain Language Summary We use high resolution images to identify submillimeter-to-centimeter scale features that resulted from either primary deposition or alteration of the rocks after the sediment was deposited at Vera Rubin ridge (VRR). VRR is located on the flank of Aeolis Mons, the 5-km high mound that occupies the center of Gale crater on Mars. We find that the majority of these fine-scale features were created after the initial deposition of sediment, when water existed in the subsurface and interacted with and altered the rocks. A subset of these features is dark gray in color and have iron-rich compositions that suggest iron remobilization and recrystallization within the host rock. We find that rocks with larger grain sizes also show more postdepositional alteration features, suggesting that grain size influenced where water moved and interacted with rocks in the subsurface.

1. Introduction

Vera Rubin ridge (VRR) is a linear, topographically high feature that parallels the northwestern perimeter of lower Aeolis Mons (informally, Mt. Sharp) in Gale crater, Mars (Figure 1; Anderson & Bell, 2010). From orbital data, VRR is distinct from the subjacent and superjacent rocks in that it shows a strong spectral absorption attributed to hematite (Fraeman et al., 2013). However, from *Curiosity* images, the rocks in VRR are laminated mudstone like the underlying strata (Edgar et al., 2020). Rocks within the ridge are inferred to have been deposited in lacustrine environments, similar to the Mt. Sharp rocks below (Edgar et al., 2020;

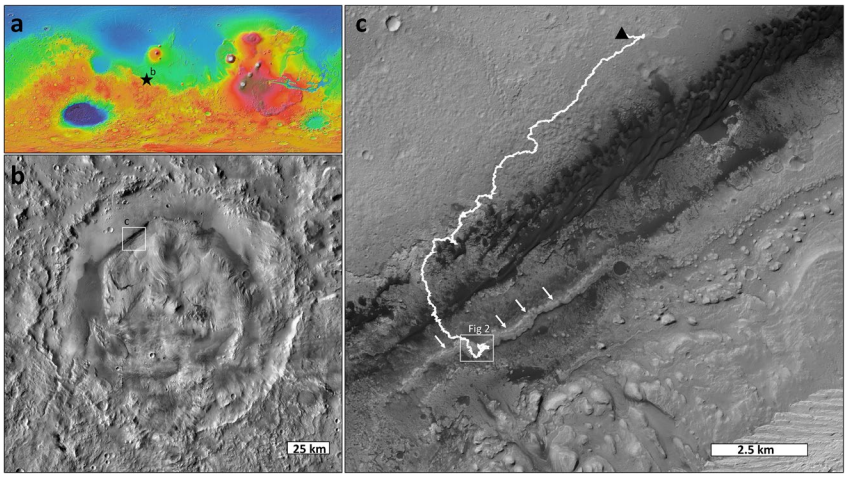


Figure 1. (a) Global Mars Orbiter Laser Altimeter (MOLA) elevation map of Mars (Smith et al., 2001), with a black star showing the location of Gale crater. (b) Thermal Emission Imaging System Visible Imaging Subsystem (THEMIS-VIS) grayscale mosaic of Gale crater (Bennett et al., 2018), showing the region of exploration along the NW margin of Mt. Sharp. (c) Context Camera (Bell et al., 2013) image showing the MSL traverse area (P22_009571_1756_XI_04S222W). The black triangle shows the location of the landing site, the white line shows the rover traverse up to sol 2,257, and the white arrows point to VRR. MSL, Mars Science Laboratory; VRR, Vera Rubin ridge.

Grotzinger et al., 2015). The Mars Science Laboratory (MSL) team has been using data acquired using the *Curiosity* rover to reconstruct the geologic history of rocks exposed on VRR. Combined, the textural, chemical, mineralogical, and spectral properties of VRR documented by *Curiosity* suggest a regional-scale, late-stage diagenetic event(s) led to increased cementation and mineral recrystallization of the area, and this is the reason for the erosional resistance of VRR and unique spectral properties in orbital data (Fraeman et al., 2020, and references therein).

The analysis of fine-scale features and textures within these sedimentary facies can reveal important information about both primary and secondary processes. The size, distribution, sorting, and orientation of grains all contribute to understanding the depositional processes. Diagenetic indicators such as the degree of cementation of the rock and the presence of crosscutting, later diagenetic features can help characterize the postdepositional history of fluid flow (e.g., Chan et al., 2005; Mozley & Davis, 2005; Potter et al., 2011; Raiswell & Fisher, 2000). The distribution and composition of diagenetic features may help constrain the fluid motion, fluid chemistry, the redox environment, and the number and relative timing of diagenetic events (Beitler et al., 2005; Chan et al., 2000, 2005).

Here, we constrain the number and timing of diagenetic events at VRR and diagenetic fluid pathways by analyzing fine-scale (mm-to cm-scale) features using images acquired by *Curiosity*'s Mars Hand Lens Imager (MAHLI). We summarize observations of fine-scale features and characterize their stratigraphic distribution through VRR. While we describe fine-scale features that result from both primary and secondary processes (Edgar et al., 2020), in this volume, provides an in-depth discussion of the depositional environments under which VRR rocks were emplaced. This manuscript focuses on fine-scale features and their implications for the diagenetic history of VRR and implications for its regionally enhanced topographic expression.

1.1. The *Curiosity* Rover in Gale Crater

The *Curiosity* rover on the MSL mission landed in Gale crater (~155-km diameter) in August 2012. Gale crater is located on the martian dichotomy boundary (Figure 1a), and contains an ~5 km high layered mound, informally called Mt. Sharp (Figure 1b). Gale crater was selected as the MSL landing site, in part, because Mt. Sharp shows stratigraphic changes in mineralogy, observable from orbit, that are inferred to record a transition from more water-rich environments conducive to clay-mineral formation to more water-poor environments conducive to the precipitation of evaporative sulfate minerals (Milliken et al., 2010; Thomson et al., 2011).

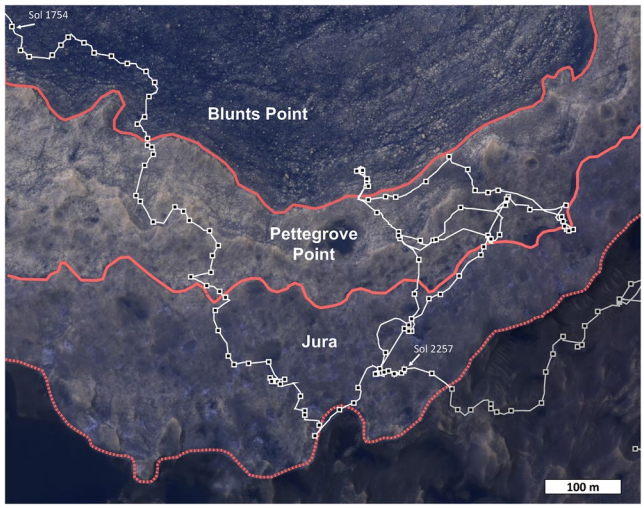


Figure 2. Context for the *Curiosity* rover traverse across Vera Rubin ridge. Background: HiRISE image ESP_042682_1755_COLOR. Image is oriented with north at the top. The white line shows the rover traverse, with stopping locations marked by black points. Solid red lines show the stratigraphic member boundaries. The area south of the Jura member (shaded black) is the clay-bearing Glen Torridon region that *Curiosity* explored after exploration of VRR. The dotted red line shows the geomorphic boundary between VRR and Glen Torridon. HiRISE, High Resolution Imaging Science Experiment; VRR, Vera Rubin ridge.

Between sol 0 (August 2012) and sol 2,258 (December 2018, the last sol covered in this paper), *Curiosity* drove almost 20 km and traversed a series of stratigraphic units that define key depositional environments within Gale crater. The Murray formation comprises the stratigraphically lowest (i.e., oldest) exposed stratal package of Mt. Sharp. The >300-m thick Murray formation displays a relatively restricted range of facies, consisting primarily of laminated mudstone interbedded with intervals of cross-bedded sandstone (Edgar et al., 2020; Grotzinger et al., 2015; Rivera-Hernández et al., 2020; Stack et al., 2019). The Murray formation's laminated mudstones are interpreted to have been deposited in a lake or lake margin environment with minor contribution from shoreline eolian and fluvial processes (Edgar et al., 2020; Grotzinger et al., 2015; Rivera-Hernández et al., 2020; Stack et al., 2019).

Strata of the Murray formation have also experienced a complex postdepositional history (Frydenvang et al., 2017; Kah et al., 2018; Kronyak et al., 2019; Nachon et al., 2017; Sun et al., 2019). Gypsum-bearing veins are the most widespread diagenetic feature in Gale crater. The majority of veins are gypsum bearing, but enrichments in Mg, Fe, and K have been observed in halos around some nonmineralized fractures and veins that contain discrete episodes of dark gray mineralization (Kronyak et al., 2019; L'Haridon et al., 2018; Nachon et al., 2017), which indicate multiple episodes of diagenetic fluid flow. Lenticular features in the lowermost Murray formation have been interpreted as pseudomorphs after early diagenetic calcium sulfate deposition (Kah et al., 2018) that may have contributed to subsurface brines responsible for gypsum-bearing veins. Elsewhere in the Murray formation, a variety of early to late diagenetic nodular features are the most prevalent indicators of postdepositional fluid flow (Minitti et al., 2019; Nachon et al., 2017; Sun et al., 2019).

1.2. Vera Rubin Ridge

Analyses of sedimentary facies within VRR show fine-grained, finely laminated strata that have been interpreted to represent a vertical continuation of Murray formation lacustrine deposits (Edgar et al., 2020). Before reaching VRR, *Curiosity* traversed upward through Murray formation strata defined as the Blunts Point member (Figure 2). The Blunts Point member has been interpreted to also consist of lacustrine deposits, although many white veins crosscut the strata making the primary strata difficult to observe (Edgar et al., 2020). Within VRR, two stratigraphic members of the Murray formation are exposed: the Pettegrove Point member and the Jura member, which occurs both topographically and stratigraphically above the Pettegrove Point member. Figure 2 shows a High Resolution Imaging Science Experiment (HiRISE) image of the portion of VRR explored by *Curiosity* and is annotated with the boundaries of these members. Boundaries are defined by subtle changes in color, grain size, and texture of lacustrine deposits, and extrapolated beyond *Curiosity*'s traverse using topographic and morphologic expression visible from orbit (Edgar et al., 2020). The bottom of Figure 2 (south of VRR) shows the geomorphic contact between VRR and the clay-mineral-bearing Glen Torridon area. While this contact marks a geomorphic boundary between a ridge (VRR) and a topographic low (Glen Torridon), it is not intended to indicate a boundary between process-defined geologic units. The *Curiosity* rover explored Glen Torridon after leaving VRR, therefore, analysis of Glen Torridon is outside the scope of our study. *Curiosity* crossed the Blunts Point-Pettegrove Point and the Pettegrove Point-Jura member boundaries multiple times during the VRR campaign (Figure 2; Fraeman et al., 2020). Multiple transects show that member boundaries do not strictly follow elevation contours (Edgar et al., 2020); this is considered when comparing data from the multiple traverses.

2. Data Sets and Methods

2.1. Mars Hand Lens Imager (MAHLI)

In this research, we analyze fine-scale (submm-to-cm size) depositional and diagenetic features that are visible in MAHLI images (Edgett, 2013a, 2013b). MAHLI is a color camera (Edgett et al., 2012) mounted on the turret at the end of the *Curiosity* rover's robotic arm (Robinson et al., 2013). The arm places the camera close to a given geologic target to acquire images to investigate grain size and grain-scale features and textures similar to observations through a geologist's hand lens. At the closest standoff distance (~1 cm), resulting images have a scale of ~17 μm/pixel (Edgett et al., 2012). MAHLI images are typically obtained as a set at each target. The standard suite of observations include images from 25 cm standoff (~100 μm/pixel) to provide context, 5 cm standoff (~31 μm/pixel) to provide an intermediate resolution designed to be comparable in scale to the Mars Exploration Rover Microscopic Imager (Edgett et al., 2012; Herkenhoff et al., 2003), plus the closest possible standoff for detailed analysis. In all cases, standoff distance is defined as the distance between the target and a plane defined by the MAHLI contact sensor probes. Regardless of standoff distance, it takes ~3 pixels to enable a confident detection of features in MAHLI images.

We analyze MAHLI images from 158 different targets on and just below VRR acquired between sols 1,734 and 2,258. Of these targets, 27 are from the uppermost portion of the Blunts Point member and the remaining from the Pettegrove Point and Jura members. For this paper, we do not interpret the entire Blunts Point member, but instead include these targets for comparison with targets within the Pettegrove Point and Jura members. MAHLI images that were taken at nonbedrock targets, including eolian sand ripples, an irregular cluster of float rocks investigated between sols 2,016 and 2,022 (Fraeman et al., 2020), or rover hardware (e.g., wheel imaging, calibration targets; e.g., Yingst et al., 2020) are not included in this manuscript. Finally, although images are often centered around a specific target within the image scene; here, we analyze everything that is visible within each MAHLI image; when more than one image focused on the same area, we count those as a single target.

Within bedrock images, we describe the presence or absence of a discrete suite of features: continuous lamination, nodules, veins, crystal features, star-shaped pits, and various dark gray features (see Section 4.1). The relative color of materials is also noted. Interpreting color in MAHLI images can be affected by the lighting conditions (i.e., full sun, full shadow, partial shadow; Edgett et al., 2015). Since the color is not spectrally characterized, the reported color is qualitative and relative. We also note that the 2018 global dust event occurred during VRR campaign (Guzewich et al., 2019), during which the dust suspended in the atmosphere caused all images to take on an orange/red hue. We use color stretched images (i.e., using the "autotone" tool in Adobe Photoshop) taken during the dust storm to make broad interpretations of relative color categories (e.g., red vs. gray).

2.2. ChemCam and the Gini Index

The Chemistry and Camera (ChemCam) instrument suite is mounted on *Curiosity*'s remote sensing mast (Warner et al., 2016) and is designed to characterize the composition of rocks near the rover remotely (Le Mouélic et al., 2015; Maurice et al., 2012; Wiens et al., 2012). ChemCam consists of a Laser-Induced Breakdown Spectrometer (LIBS) and a Remote Micro-Imager (RMI). In addition to providing compositional information about a given geological target, the LIBS laser (Wiens, 2013) can be used to estimate rock grain size using the Gini index mean score (G_{MEAN}) as a proxy (Rivera-Hernández et al., 2019, 2020). We discuss the composition of only one ChemCam LIBS target in this work. For an in-depth discussion of the chemistry of many of the features of this study, we refer the reader to L'Haridon et al. (2020). The G_{MEAN} quantifies the compositional variability between ChemCam LIBS points for each rock target. A ChemCam observation typically consists of a raster, which is a line or grid of 5–10 points (~0.4–0.6 mm in diameter) that are typically spaced 6 mm from each other for targets at 3-m distance. At each point, the ChemCam LIBS laser typically shoots 30 pulses, with the first laser shots removing surface dust and coatings (Wiens et al., 2012, 2013). Assuming compositional homogeneity at the scale of the ChemCam raster, rocks with grains smaller than the LIBS spots (medium to coarse sand in size) yield smaller point to point variability and therefore a lower G_{MEAN}, whereas targets with grains about the size or larger than the LIBS spots have a higher variability and a higher G_{MEAN} (Rivera-Hernández et al., 2019). To estimate the grain size in VRR

Journal of Geophysical Research: Planets

10.1029/2019JE006311

Table 1

Results From This Study Showing the Characteristics of Each Target Analyzed (Bennett, 2021)

Target Name	Sol (first occurrence)	Elevation (m)	Member (Blunts Point, Pettegrove Point, Jura)	Continuous laminations	Nodules and/or Concretions	Light Toned Crystal Psuedomorphs	Mixed Tone Crystal Psuedomorphs	Star-shaped pits	Dark gray surface features	Dark gray vein associated features	Dark gray fracture embedded features	Dark gray prismatic features	Color	DRT scratches (Deep, Shallow, None)	G_MEAN	G_MEAN STDV	Gini index grain size estimates	Comments
Pecks_Point	1734	-4246	Blunts Point	X	X								Red					
McFarland_Mountain	1736	-4246	Blunts Point		X				X				Red					
Winter_Harbor	1736	-4246	Blunts Point	X	X				X				Red	Deep				
Rice_Point	1739	-4245	Blunts Point										Red					
Mingo	1744	-4243	Blunts Point										Red	Deep				
Jobbies	1745	-4243	Blunts Point		X				X				Red					
Appledore	1747	-4240.5	Blunts Point										Red					
Tupper_Ledge	1748	-4239	Blunts Point						X				Red					
Foxbird	1753	-4237.5	Blunts Point		X								Red					
Pond_of_Tea	1783	-4225	Blunts Point		X				X				Red					
Burnt_Coat	1783	-4225	Blunts Point		X					X			Red					
Emery_Cove	1786	-4226	Blunts Point		X								Red					
Agamenticus	1795	-4222.5	Blunts Point		X								Red		0.02	0.00	mud	
Tinker	1796	-4219.5	Blunts Point						X				Red					
Doliver	1797	-4216.5	Blunts Point		X								Red					
Abagadasset	1797	-4217	Blunts Point										Red					
Bauneg_Beg	1800	-4213.5	Blunts Point		X				X				Red					
Tyler	1802	-4208.5	Blunts Point										Red		0.02	0.01	mud	
Robinson_Rock	1806	-4206.5	Pettegrove Pt		X				X				Red	Deep				
Chamberly	1809	-4202	Pettegrove Pt		X								Red		0.07	0.01	mud to coarse silt/very fine sand	
Mount_Ephraim	1811	-4199	Pettegrove Pt	X							X		Purple		0.03	0.00	mud	
Kemps_Folly	1811	-4198.5	Pettegrove Pt	X						X			Purple		0.02	0.00	mud	
Sasanoa	1811	-4199.5	Pettegrove Pt	X						X			Purple	Deep	0.01	0.01	mud	
Pumpkin_Nob	1814	-4198	Pettegrove Pt										Red		0.02	0.01	mud	
Schoppee	1816	-4196	Pettegrove Pt	X							X		Red					
Christmas_Cove	1818	-4196.5	Pettegrove Pt	X									Red	Shallow				
Whittum	1818	-4196.5	Pettegrove Pt	X							X		Red					
Mitten_Ledge	1818	-4196.5	Pettegrove Pt	X							X		Red	Shallow				
Passadumkeag	1821	-4195	Pettegrove Pt		X	X			X				Red	None				
Pennessewassee	1821	-4195	Pettegrove Pt		X						X		Red					
Sherwood_Forest	1824	-4191	Pettegrove Pt		X								Tan	Shallow				No veins
Troll_Valley	1824	-4191	Pettegrove Pt		X								Dusty					
Enon	1829	-4186	Pettegrove Pt		X								Dusty					
Collingham	1830	-4187	Pettegrove Pt		X								Dusty					
Katberg	1834	-4184.5	Pettegrove Pt		X								Red					
Lucknow	1836	-4182	Pettegrove Pt								X		Red	None				
Ecca	1836	-4182	Pettegrove Pt								X		Red	None	0.04	0.00	mud	
Duitschland	1838	-4180	Pettegrove Pt		X								Red		0.04	0.00	mud	
Cheshire	1838	-4180.5	Pettegrove Pt		X								Dusty		0.03	0.01	mud	
Stormberg	1845	-4180	Pettegrove Pt										Red					
Blinkberg	1850	-4176.5	Pettegrove Pt										Red					No veins
Balfour	1852	-4173.5	Pettegrove Pt		X								Red		0.01	0.00	mud	
Sibasa	1863	-4173.5	Pettegrove Pt			X							Red	Shallow				
Gamka	1863	-4174	Pettegrove Pt					X					Red					
Barberton	1865	-4174.5	Pettegrove Pt		X					X			Red					
Campbellrand	1865	-4174.5	Pettegrove Pt								X		Red					
Volksrust	1868	-4172	Pettegrove Pt		X								Dusty					
Waboomberg	1870	-4170	Pettegrove Pt							X	X		Red					
Platberg	1870	-4170	Pettegrove Pt										Red	None	0.02	0.01	mud	
Middleton	1875	-4167.5	Jura (Red)			X							Red					
Fort_Brown	1875	-4168	Jura (Red)	X		X		X			X		Red	None	0.02	0.00	mud	
Zululand	1879	-4166.5	Jura (Gray)	X									Gray					
Hexriver	1879	-4166.5	Jura (Red)						X				Red	None				
Klippan	1886	-4166.5	Jura (Red)				X						Red	None	0.07	0.01	mud to coarse silt/very fine sand	
Klipfonteinheuwel	1886	-4166.5	Jura (Gray)	X									Gray					
Lyttelton	1889	-4163.5	Jura (Red)			X					X		Red					
Strubenkop	1892	-4158	Jura (Gray)	X			X			X			Gray					
Drakensberg	1892	-4158	Jura (Red)	X			X	X		X	X		Red	None	0.05	0.01	mud	ChemCam target that gives the GINI index is Pongola, close to MAHLI target Drakensburg
Mzamba	1895	-4157	Jura (Red)	X							X		Red		0.05	0.00	mud	
Muck	1897	-4157	Jura (Gray)	X									Gray		0.05	0.00	mud	
Wick	1897	-4157	Jura (Red)	X		X		X					Red					

Journal of Geophysical Research: Planets

10.1029/2019JE006311

Table 1
Continued

Talisker	1904	-4154	Jura (Gray)	X	X					X		X	Gray					
Oban	1904	-4154.5	Jura (Gray)		X		X			X			Gray	None	0.04	0.01	mud	
Haddo_House	1906	-4152.5	Jura (Red)						X				Red					
Holyrood	1906	-4152.5	Jura (Red)			X				X	X		Red		0.06	0.01	mud	
Ben_Loyal	1911	-4155	Jura (Gray)		X				X	X		X	Gray		0.07	0.01	mud to coarse silt/very fine sand	
Raasay	1922	-4154	Jura (Gray)		X		X					X	Dusty (Gray?)					
Haroldswick	1922	-4154	Jura (Gray)									X	Gray					
Crinan	1925	-4153	Jura (Gray)	X									Gray					
Assynt	1925	-4153	Jura (Gray)	X									Gray					
Elgin	1925	-4152.5	Jura (Red)	X									Red		0.04	0.00	mud	
Jura	1926	-4153	Jura (Gray)	X			X			X			Gray		0.08	0.01	coarse silt/vfs	
Craighead	1927	-4153	Jura (Gray)		X			X	X	X			Gray	None				
Barra	1927	-4153	Jura (Red)	X					X	X			Red					
Banff	1929	-4150	Jura (Gray)				X	X	X				Gray		0.08	0.01	coarse silt/vfs	
Unst	1931	-4149	Jura (Gray)				X		X	X	X		Gray	Deep				
Funzie	1932	-4149	Jura (Gray)	X			X	X	X	X		X	Gray					
Aberfoyle	1932	-4149	Jura (Gray)					X	X	X		X	Gray		0.10	0.01	coarse silt/vfs	
Canna	1932	-4149	Jura (Gray)		X		X		X	X		X	Gray					Bleached halo around crystal psuedomorphs
Ross_of_Mull/ Rona	1934	-4149	Jura (Gray)	X	X				X	X		X	Gray	Deep	0.06	0.02	mud	ChemCam target is Rona
Macleans_Nose	1934	-4149	Jura (Gray)		X				X				Gray					
Langholm	1934	-4149	Jura (Gray)		X				X	X			Gray					
Wanlockhead	1935	-4149	Jura (Gray)	X	X		X	X		X			Gray					
Rhum	1935	-4149	Jura (Gray)		X			X	X	X			Gray					
Loch_Maree	1937	-4149	Jura (Gray)		X				X	X		X	Gray					
Mallaig	1940	-4148	Jura (Red)										Red					
Knoydart	1940	-4148	Jura (Red)										Red					
Eaval	1943	-4148	Jura (Gray)		X								Gray					
Loch_Gairloch	1945	-4147	Jura (Red)					X					Red					
Balmedie	1950	-4146.5	Jura (Gray)						X	X			Gray	None				
Skara_Brae	1954	-4146	Jura (Red)	X		X	X			X	X		Red		0.08	0.01	coarse silt/vfs	
Glen_Roy	1954	-4146	Jura (Red)	X		X		X			X		Red		0.04	0.01	mud	
Arnaboll	1960	-4146	Jura (Red)	X							X		Red		0.03	0.01	mud	
Glenfinnan	1961	-4146	Jura (Red)	X		X							Red		0.09	0.01	coarse silt/vfs	
Newmachar/ Lake Orcadie	1963	-4146.5	Jura (Gray)		X				X	X			Gray	None				Unsuccessful drill attempt
Yesnaby	1963	-4146.5	Jura (Gray)		X				X	X			Gray					
Forties	1966	-4146.5	Jura (Gray)		X				X	X		X	Gray					
Rockall	1975	-4146.5	Jura (Gray)		X				X				Dusty (Gray?)					
Benbecula	1975	-4146.5	Jura (Gray)							X			Gray					
Lake_Orcadie2	1979	-4147	Jura (Gray)		X				X	X			Gray					
North_Harris	1988	-4150.5	Jura (Red)	X							X		Red					
Barkeval	1988	-4150.5	Jura (Red)	X									Red					
Seaforth_Head	1991	-4152	Jura (Red)				X						Dusty (Red?)					
Stirling_Castle	1993	-4152	Jura (Red)				X						Dusty					
Paisley	1996	-4153.5	Jura (Red)			X							Red					
Durness	1996	-4153.5	Jura (Red)				X						Red	None				
Sgurr_of_Eigg	2000	-4159	Pettegrove Pt		X						X		Red	None				
Appin	2001	-4159	Pettegrove Pt		X						X		Red					
Brora	2001	-4159	Pettegrove Pt		X								Red	None	0.09	0.01	Coarse silt/vfs	ChemCam target that gives the GINI index is Boddam, close to MAHLI target Brora
Stranraer	2005	-4165	Pettegrove Pt	X									Red	None				
Murchison	2005	-4164.5	Pettegrove Pt						X				Dusty (Red?)					
Lanark	2008	-4165	Pettegrove Pt						X	X	X		Red	None				
Dun_Caan	2008	-4160.5	Pettegrove Pt	X							X		Red		0.05	0.00	mud	
Lingarabay	2013	-4165	Pettegrove Pt		X								Red	Shallow	0.04	0.01	mud	
Kinloch	2013	-4155	Pettegrove Pt		X								Red					
Corsehill	2014	-4155	Pettegrove Pt		X								Dusty (Red?)					
Babbitt	2029	-4166	Pettegrove Pt						X				Red		0.04	0.01	mud	
Pokegama	2032	-4166.5	Pettegrove Pt								X		Red		0.01	0.00	mud	
Nashwauk	2038	-4181	Pettegrove Pt	X							X		Red		0.03	0.00	mud	
Bald_Eagle_Lake	2042	-4179.5	Pettegrove Pt										Red	Shallow	0.02	0.00	mud	
Pigeon_River	2044	-4179.5	Pettegrove Pt	X									Red	Shallow	0.02	0.01	mud	
Bilbert	2048	-4188	Blunts Point		X				X				Red	Deep				
Giants_Range	2048	-4188	Blunts Point		X				X				Red	Shallow				
Culver	2049	-4188.5	Blunts Point		X				X				Red					
Floodwood	2049	-4188	Blunts Point		X								Red	Deep				No veins
Carleton	2049	-4188	Blunts Point		X				X				Red					

Journal of Geophysical Research: Planets

10.1029/2019JE006311

Table 1
Continued

Duluth	2055	-4191.5	Blunts Point		X				X				Red	Deep	0.02	0.00	mud	Drill Hole
Side Lake	2082	-4187.5	Blunts Point		X				X				Red					
Tofte	2083	-4192	Blunts Point						X				Red					
Deerwood	2083	-4191.5	Blunts Point		X								Red					
Dumbarton_Rock	2102	-4164.5	Pettegrove Pt		X		X						Red	None	0.10	0.01	mud	
Duntarvie_Castle	2102	-4164	Pettegrove Pt			X							Red					
Duntelchaig	2102	-4164	Pettegrove Pt						X				Red					
Chippewea	2107	-4165.5	Pettegrove Pt		X						X		Red					
Orr	2108	-4164	Pettegrove Pt						X		X		Red					
Voyageurs	2109	-4164.5	Pettegrove Pt						X				Red	None				Unsuccessful drill attempt
Walsay	2119	-4158.5	Pettegrove Pt								X		Red					
Alisa Craig	2121	-4159	Pettegrove Pt		X								Red	None				Unsuccessful drill attempt
Diabaig	2127	-4162.5	Pettegrove Pt	X		X			X		X		Red					
Slioch	2127	-4162.5	Pettegrove Pt			X			X		X		Red		0.03	0.01	mud	
Scourie_More	2132	-4169.5	Pettegrove Pt		X					X			Gray					Gray target in Pettegrove Point
Dobbs_Linn	2132	-4169.5	Pettegrove Pt		X								Red	Shallow				
Mount Battock	2132	-4169.5	Pettegrove Pt		X								Gray					Gray target in Pettegrove Point
Stoer	2134	-4170.5	Pettegrove Pt		X								Red	Deep				Drill Hole
Tayvallich	2161	-4155.5	Pettegrove Pt								X		Red		0.08	0.00	coarse silt/vfs	
Trollochy	2166	-4149.5	Jura (Red)				X		X	X			Red					
Portobello	2166	-4149.5	Jura (Gray)		X		X		X	X			Gray					Bleached halos present
Burn_O_Vat	2166	-4149.5	Jura (Gray)		X		X		X	X			Gray					
Inverness	2168	-4150.5	Jura (Gray)		X		X		X	X			Gray	None	0.10	0.01	coarse silt to very fine sand	Unsuccessful drill attempt
Grange	2217	-4150.5	Jura (Gray)				X			X			Gray					
Lossiemouth	2218	-4150.5	Jura (Gray)				X		X	X			Gray					
Calgary	2220	-4150.5	Jura (Gray)				X		X	X			Gray	Shallow				
Findon	2220	-4150.5	Jura (Gray)		X				X	X			Gray					
Highfield	2223	-4146.5	Jura (Gray)		X		X		X	X			Gray	Shallow				Drill Hole
Woodhill	2254	-4145	Jura (Red)								X		Red	None	0.07	0.01	mud to coarse silt/very fine sand	
Springhill	2254	-4145	Jura (Red)			X		X					Red					
Corrieshalloch_Gorge	2258	-4144	Jura (Red)								X		Red					
Rock_Hall	2258	-4144	Jura (Red)								X		Red					Drill Hole

For each target we include: the first sol MAHLI images were taken of the target, the elevation of the target, the stratigraphic member the target belongs to Edgar et al. (2020), the presence ("X") or absence (empty cell) of several features, the color of the target, whether the Dust Removal Tool created scratches in the target, grain size estimates for a subset of twhe targets (Rivera-Hernández, 2020a, 2020b), and any relevant comments.

rocks, we used a G_{MEAN} grain size scale that was calibrated using the G_{MEAN} of Murray formation rocks with known grain size (Rivera-Hernández et al., 2020). The grain size for the calibration rocks were visually measured and classified by Rivera-Hernández et al. (2020) using the Wentworth scale (Wentworth, 1922), where very fine sand = 62.5–125 μm, fine sand = 125–250 μm, medium sand = 0.25–0.50 mm, and coarse sand = 0.50–1.00 mm. Clay and silt sizes were grouped together and classified as mud (62.5 μm and smaller), in which coarse silt is 20.0–62.5 μm. A mud grain size was inferred for targets that did not have resolvable grains in MAHLI images (<62.5 μm, coarse silt).

G_{MEAN} results are reported in Table 1 using Wentworth grain-scale nomenclature (Wentworth, 1922). In this scale, mud (clay size through medium silt size) has a G_{MEAN} of 0.00–0.07, coarse silt to very fine sand has a G_{MEAN} of 0.07–0.10, and very fine to medium sand has a G_{MEAN} of 0.11–0.16. Rocks with G_{MEAN} = 0.07 are at the boundary between mud and coarse silt to very fine sand and are reported here as mud to coarse silt/very fine sand (Rivera-Hernández, 2020a, 2020b; Rivera-Hernández et al., 2020). While we use the Wentworth scale nomenclature to refer to different grain sizes, the G_{MEAN} grain size ranges were defined in the calibration procedure and reflect quantitative trends between G_{MEAN} and resolvable grain sizes in Murray formation rocks (i.e., grains of a certain size have narrow G_{MEAN} values).

To ensure that the quantified chemical variability of the LIBS data can be attributed to variation in grain size, LIBS shots on or near visible diagenetic features, loose sediment, and fractures/cracks are removed from the Gini index mean score analysis (Rivera-Hernández et al., 2019, 2020). The suite of ChemCam targets and MAHLI targets on VRR do not always overlap; this is important because the ChemCam results, therefore, extend the range of observations beyond that of MAHLI imaging alone. All ChemCam LIBS targets on VRR are investigated even if they do not include a corresponding MAHLI observation.

3. Fine-Scale Features in VRR Rocks

Curiosity traversed across VRR multiple times, which resulted in a complex path (Figure 2). Our analysis considers both position within the member (relative to boundaries) and elevation (Table 1). The elevation is rounded to the nearest half meter and is defined relative to the Mars areoid (Smith et al., 2001). For a com-

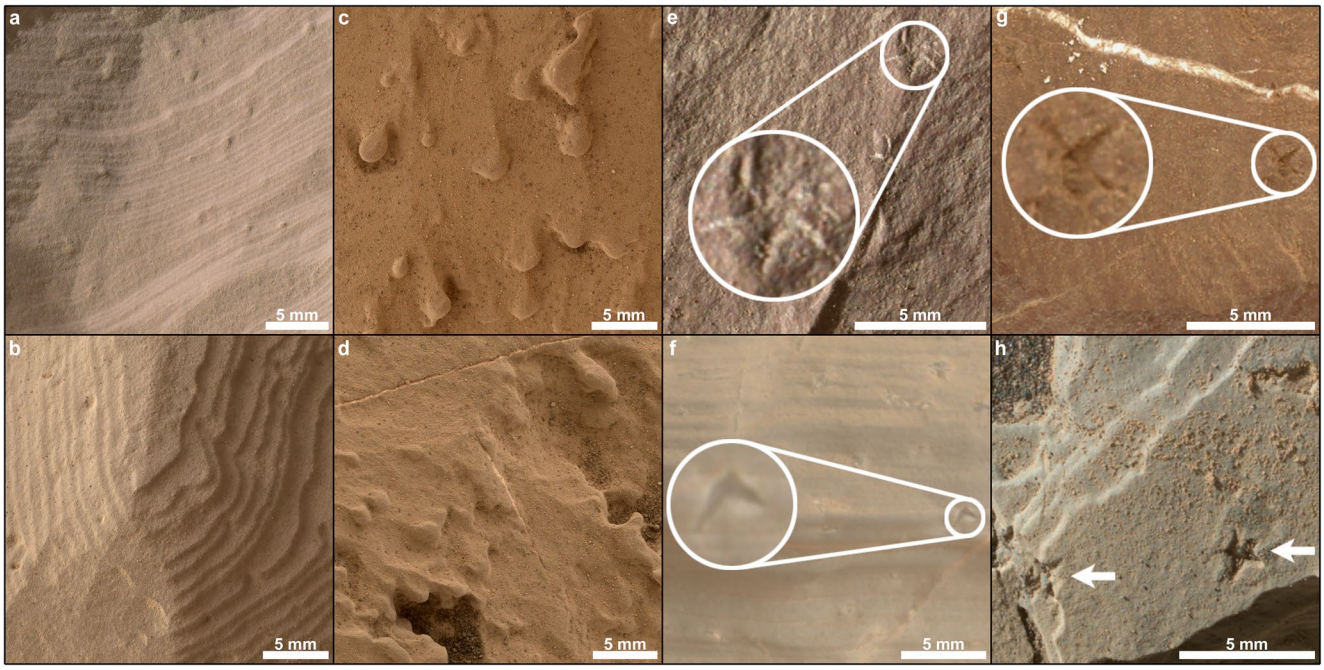


Figure 3. MAHLI images showing a variety of fine-scale features. (a) Continuous lamination, target Schoppee; (b) continuous lamination, Whittum; (c) nodules, Enon; (d) nodules, Volksrust; (e) crystal features, Sibasa, with magnified inset; (f) crystal features, Jura, with magnified inset; (g) star-shaped pits, Fort_Brown, with magnified inset; (h) star-shaped pits (arrows), Aberfoyle. MAHLI, Mars Hand Lens Imager.

plete list of results from individual targets, see Table 1; e.g., of each feature, see Figures 3 and 4. For each target that is included in the figures, the name is noted in the caption and the image number is included in supporting information.

3.1. Description and Interpreted Origin of Fine-Scale Features

3.1.1. Continuous Lamination

Targets are identified as containing continuous laminations when laminae are clearly visible and are undisrupted by diagenetic features such as nodules and veins (e.g., Figures 3a and 3b). In these examples, diagenetic features can crosscut the lamination as long as the laminations are still clearly visible and show no morphologic disruption. The average lamina thickness of targets on VRR ranges from 0.22 to 0.59 mm (Edgar et al., 2020), and fine-scale, parallel lamination is interpreted to represent deposition in a lacustrine environment (Edgar et al., 2020). Targets that do not exhibit fine-scale laminations are here inferred to represent observations oriented such that the laminations are not visible (e.g., looking down on a bedding surface; Figure 3e), are dust covered such that the laminations are obscured, or secondary features have overprinted the sedimentary structures (e.g., nodules; Figure 3c).

3.1.2. Nodules

Roughly spherical, positive relief features, here referred to as nodules (Figures 3c and 3d), occur in some VRR rocks. These nodules generally exhibit similar colors and textures as the host rock, but are sometimes darker gray. Here, we identify nodules embedded or attached to the rock, as opposed to spherical pebbles or potential nodules that have eroded out of the host rock and are considered to be float rock. Nodules are inferred to be diagenetic features that formed during postdepositional water-rock interaction, where localized precipitation of minerals cemented the host rock (e.g., Mozley, 2003). Nodules have been previously

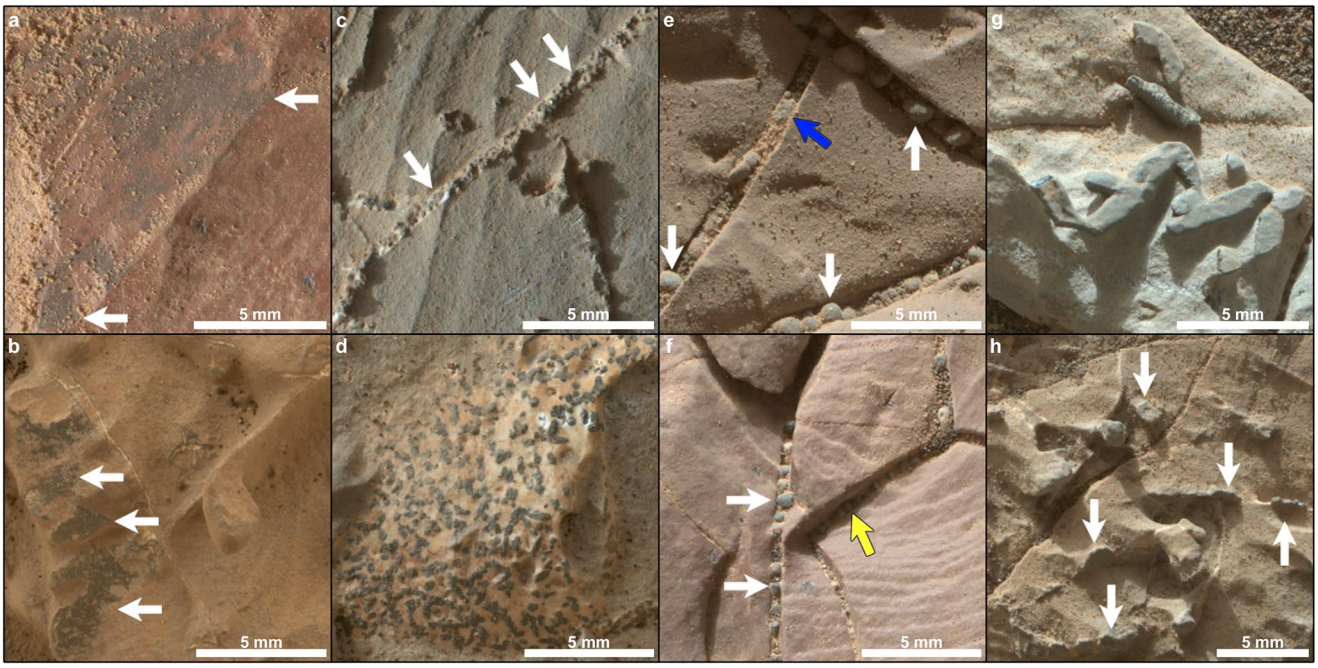


Figure 4. MAHLI images showing rock targets with dark gray features. White arrows point to the features of interest. (a) Dark gray, irregular patches in the target called Babbitt. (b) Dark gray surface features, Portobello. (c) Dark gray vein-associated mineral fill, Lake Orcadie. (d) Dark gray vein-associated features, Grange. (e) Dark gray fracture-embedded (potentially detritial) features, Mzamba. Blue arrow points to fracture-embedded features that may have been cemented together. (f) Dark gray fracture-embedded (potentially detrital) features, Dun Caan. The yellow arrow points to the ChemCam LIBS point that hit a fracture-embedded feature. (g) Dark gray prismatic forms, Haroldswick. (h) Dark gray prismatic forms, Loch Maree. MAHLI, Mars Hand Lens Imager; LIBS, Laser-Induced Breakdown Spectroscopy.

observed and documented in other regions of the Murray group (Minitti et al., 2019; Nachon et al., 2017; Sun et al., 2019), and elsewhere in Gale crater (Stack et al., 2014).

3.1.3. Veins

Veins are mineral-filled fractures that crosscut the host rock. The veins we observe in VRR rocks are typically white in color (Figure 3g), although dark gray veins occur. Veins are not included in our tabulation because veins are present in almost every MAHLI target. The few targets that do not exhibit veins are noted in the "comments" section of Table 1. Fractures observed in the Murray formation are interpreted to result primarily from hydrofracture, with mineralization by fluid flow during or after times of fracture (Kronyak et al., 2019; Nachon et al., 2017). Veins have been observed throughout *Curiosity*'s traverse (Caswell & Milliken, 2017; Kronyak et al., 2019), and previous investigations have shown that white veins in Gale crater are almost exclusively composed of calcium sulfate (Nachon et al., 2014; Rapin et al., 2016).

3.1.4. Crystal Features

Crystal features within the host rock are ~millimeters in size and appear in shapes that have discrete edges that are morphologically similar to crystal forms (e.g., lenticular, swallowtail, star, cross). For example, Figure 3e shows a morphology similar to clusters of fibrous gypsum (cf. Piñeiro et al., 2012), which commonly occur as early diagenetic features in regions of high evaporation and aridity. Similarly, the swallowtail form (Figure 3f) is also similar to morphologies observed in terrestrial examples of early diagenetic gypsum (i.e., Andeskie et al., 2018; Melezhik et al., 2005). The crystal-like features appear either as white features (i.e., Figure 3e) or mixed tone (white and dark gray) features (i.e., Figure 3f). Mixed tone features either have a dark center and white outline or white center and dark outline. Crystal features do not have a preferred orientation and appear randomly distributed throughout the host rock, which suggests formation in situ within the host material. Crosscutting host rock lamination, without destruction of lamina structures, implies that the crystal features were emplaced after the host rock was at least partially cemented or lithified (e.g., Loyd & Corsetti, 2010). L'Haridon et al. (2020) report that dark gray crystal features have compositions enriched in iron relative to the surrounding host rock and are consistent with hematite. No ChemCam LIBS observations have been made of light-toned crystal features.

The range of morphologies preserved in crystal features indicates a primary origin as early diagenetic gypsum (i.e., Figure 3h). Compositional measurements that indicate the presence of hematite in these forms suggest that these features represent later diagenetic, pseudomorphic replacement of primary gypsum, because hematite does not crystallize in a similar habit. Previous observations of lenticular crystals in the lowermost Murray formation (Kah et al., 2018) were also interpreted as pseudomorphs because the features showed a crystal habit consistent with gypsum but the rocks did not record compositions consistent with preservation of primary gypsum (Kah et al., 2018). Here, we suggest that pseudomorphic replacement would have occurred by late postdepositional fluid events, with iron sourced either locally from diagenetic recrystallization of hematite in the host rock or from further afield and transported by diagenetic fluids (Sunagawa, 1994). No chemical data were retrieved from light-toned crystal features, but given the widespread precipitation of calcium sulfate throughout the region, we assume that the light-toned material here is also calcium sulfate. Data are insufficient to determine whether calcium sulfate might be original gypsum (which exhibits both lenticular and swallowtail crystal habits) or pseudomorphic after original gypsum.

3.1.5. Star-Shaped Pits

These features are depressions in the host rock that are typically star or cross shaped (i.e., Figures 3g and 3h). Some pits on VRR are rounded, but these are not included here. Based on their shape, which is similar to the crystal features in Section 4.1.4, these features are interpreted as crystal molds, identifying where an early diagenetic crystalline phase was preferentially eroded or dissolved. Such inference is supported by the observation of a crystal feature that is also pitted (target: Banff, see Figure S1) but not completely removed. Such pitting could result from either diagenetic dissolution in the subsurface or erosion after exposure at the surface. Crystal molds have previously been identified on Mars in Meridiani Planum (McLennan et al., 2005).

3.1.6. Dark Gray Features

Fine-scale, dark gray (almost black) features frequently occur in VRR rocks. These features exhibit a variety of morphologies, so we have divided them into four categories (Figure 4). L'Haridon et al. (2020) examined the chemistry of these, and similar, features and found that the dark gray features on VRR were consistently enriched in iron relative to the host rock.

(a) Dark gray surficial features

This category includes dark gray features that comprise irregularly shaped patches that appear to occur primarily on the surface of rock outcrops. Although the discoloration of the host rock surfaces (Figure 4a) could potentially extend to depth, they commonly exhibit a smoother texture than surrounding host rock and positive relief (Figure 4b). Based on these characteristics, we interpret these features to represent either diagenetic alteration of primary host rock materials or precipitation from diagenetic fluids.

(b) Dark gray vein-associated features

This category includes dark gray vein material as well as dark gray features that are embedded or entrained in a matrix of lighter-toned vein fill (Figures 4c and 4d). Entrained features exhibit a range of polygonal shapes that suggest formation, or replacement, of distinct crystals (Figure 4d). We interpret these features to be late diagenetic in origin because of an association with veins that crosscut much of the local stratigraphy and are therefore inferred to have formed after deposition and lithification of the host materials.

(c) Dark gray fracture-embedded features

This category includes rounded, dark gray features that are embedded in unfilled fractures (Figures 4e and 4f). We consider two possible origins for these features: (1) detrital grains wedged into fractures in rocks and (2) diagenetic nodules originating within fractures. In order to test potential origins, we analyze the composition of the single ChemCam LIBS point that appeared to hit one of these features (Dun Caan target, Figure 4f). The ChemCam target was the host rock, but one of the LIBS points impinged on a fracture-embedded feature that is in shadow and therefore is difficult to see. Our analysis of this point reveals a composition consistent with Gale sand and soil targets (e.g., Cousin et al., 2017), but is unlikely to reflect loose sand or soil deposited surficially on the feature, because these are usually efficiently removed by the first few laser shots. In addition, the composition shows limited to no iron enrichment, contrary to other types of dark gray features observed on VRR (L'Haridon et al., 2020). These data suggest that these features are detrital in origin rather than diagenetic features. These specific features are typically larger than nearby sand (some close to 1 mm in diameter in sand patches composed of ~200 μm grains), are generally more uniform and dark in color (as opposed to the range of colors observed in local sand populations), are commonly spherical and occasionally glassy (Figure 5f, bottom center). In places, these anomalous features appear to be joined to each other or to fracture walls by a lighter toned, cementing material (see blue arrow in Figure 4e). The most parsimonious explanation for these features is that they represent coarse-grained components of the local eolian bedload that have been wedged into substrate fractures. The glassy, spheroidal nature of some of these features suggests an origin as impact spherules, which are commonly associated with detrital sand components in Gale crater and elsewhere on Mars (e.g., Minitti et al., 2013). Less spherical, rounded to subangular dark gray materials may also represent coarse-grained detritus that is locally derived, such as nodules weathered from local outcrop. Because we lack detailed geochemical data for these structures and morphological observations suggest a high likelihood that these represent detrital material with multiple origins, we include these features in further discussion only because some of these materials may represent diagenetic materials eroded from local host rock.

(d) Dark gray prismatic features

Several targets display dark gray features that appear as elongate, sometimes intersecting, rectangular prisms (Figures 4g and 4h). Most occur with the long axis oriented parallel to the exposed surface planes of the host rock (Figure 4g), although they also occur as outward growths associated with submillimeter scale fractures (Figure 4h). No view was obtained that showed the relationship of these features to lamination in the host rock. In the Haroldswick target (Figure 4g), the dimensions of this feature are roughly 5 × 1 × 0.2 mm. A closeup view of Haroldswick (Figure 4g) shows that most of these features are darker

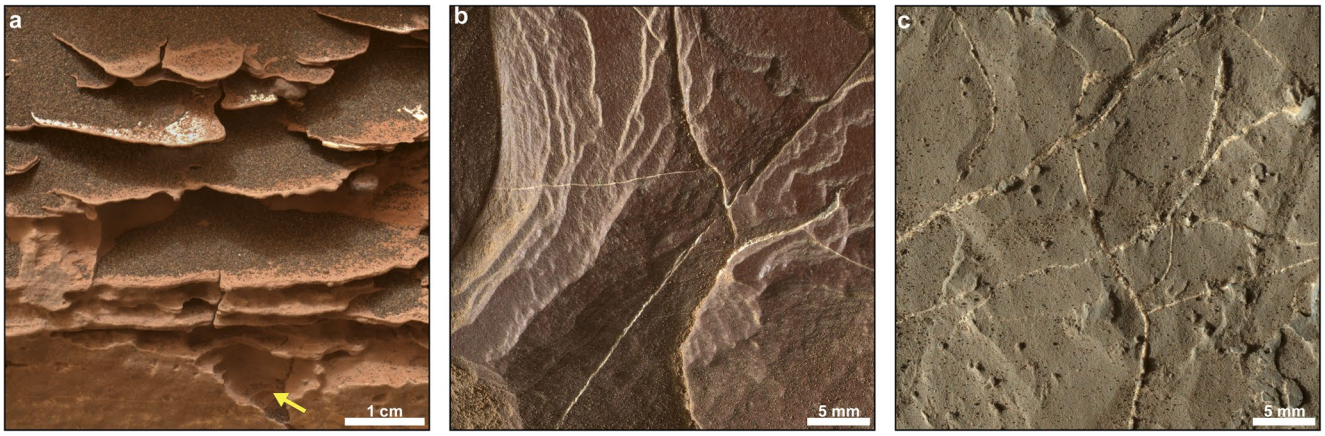


Figure 5. Different out crop expressions of veins: veins are resistant compared to the host rock (a) and recessive as compared to the host rock (b and c). (a) Blunts Point member target Side Lake. This is a view of the side of a block, and the resistant features are all interpreted to be veins. The yellow arrow points to the recessive host rock. (b) Pettegrove Point member target Stranraer. Typical top down view. Several thin white veins cut across the host rock. (c) Jura member target Lake Orcadie Sample Discard Site. Multiple veins cross cut the host rock. Some veins contain dark gray features.

than the host rock and shows a metallic sheen along recent fractured surfaces, which supports a potential hematitic composition. The rectangular prismatic form of these features is similar to crystal forms, although the rough, or granular, surface texture suggests that they are either not individual crystals, or are crystals that are undergoing surficial erosion or pitting. The granular surface texture could also represent growth of a finely crystalline secondary phase that pseudomorphically replaced a previous crystal form, or possibly the presence of substrate grains incorporated within the prismatic forms.

We suggest that the prismatic features formed in association with fluids in the fine-scale fractures and may represent poikilotopic crystal growth, where coarse crystals of the cement enclose smaller grains. Similar macroscopic crystalline clusters have been found elsewhere in the Murray formation (Kronyak et al., 2019) and are inferred to represent fluids that permeated the sedimentary substrate, resulting in mineral growth that incorporated elements from the fine-grained matrix. Such a scenario is supported by apparent initiation and outward growth of prismatic forms from fine-scale fractures (Figure 4h), as well as the granular surface texture of the crystal forms, which may reflect incorporation of host rock materials. Erosional resistance of these materials relative to the host rock and associated light-toned vein material would explain the presence of these features at the exposed surfaces of the host rock.

As noted above, dark gray features in the VRR region record a variety of morphologies. We hypothesize that these features are linked by formation through similar postdepositional fluid processes involving iron mobility. These dark gray features also suggest a continuum of diagenetic mineralization. Within fractures, this continuum is portrayed by fractures filled with only with calcium-sulfate, fractures containing both light-toned and dark gray crystalline features (Figure 4d), to dark-toned fracture-associated fill (Figure 4c), and growth that proceeds outward from fractures into the surrounding host rock (Figures 4g and 4h). Dark gray surface features that are distinct from the host rock (Figure 4b) may also occur when differential erosion causes dark gray features to be exposed and visible at the surface of the host rock, rather than clearly within a fracture.

3.2. Additional Host Rock Properties

Here, we describe additional host rock properties that we investigated in this study. Further discussion regarding the distribution of these properties and their implications for the geologic history (and especially diagenetic history) of VRR is in subsequent sections.

3.2.1. Color

The apparent color of each target investigated using the MAHLI is included in Table 1. The majority of VRR rocks were classified as "red" or "gray," but there were several targets that were classified as purple, tan, or dusty (meaning that dust obscured the rock so no interpretation of color was made). Red and gray targets within the Jura member are distinct and distinguishable (see Section 5.1); therefore, targets are designated as "red Jura" and "gray Jura" when noting the member. As discussed in Edgar et al. (2020), the red and gray color variations on VRR can be observed to cut across the primary bedding. Therefore, color variability on VRR is interpreted to be related to diagenetic activity. For additional, more detailed, descriptions of color variations on VRR from Mastcam multispectral analyses we refer the reader to Horgan et al. (2020).

3.2.2. Hardness

Rock hardness is defined as a measure of resistance to abrasion, or the ease with which a surface can be scratched. Several observations can be used to estimate rock hardness, including visual clues and physical tests (cf. Kronyak et al., 2020). Since VRR consists primarily of fine-grained, clay-bearing siliciclastic rocks (Edgar et al., 2020), we interpret that differential hardness is most likely related to the extent of lithification, including cementation, that occurred during diagenesis.

The first hardness test is related to variation in the outcrop expression of veins in MAHLI images of VRR rocks (Figure 5). In some locations, the veins protrude from the host rock as fins (Figure 5a) and in others the veins outcrop at the same surface level the host rock (Figures 5b and 5c). Given the similarity in white vein composition throughout *Curiosity*'s traverse (i.e., Ca-sulfate; Nachon et al., 2014; Rapin et al., 2016) and the assumption that they should have similar hardness, we interpret varying outcrop expression of the veins to be primarily a function of host rock properties. Therefore, positive relief veins indicate a softer host rock, while more recessive veins indicate a harder host rock.

Physical tests based on rover interactions with the surface, including scratching by the Dust Removal Tool (DRT), can also be used to qualitatively interpret rock hardness (cf. Kronyak et al., 2020). The DRT utilizes stainless steel wire brushes to remove dust from flat surfaces (Figure 6). The DRT brushes are moved in circular motions to wipe the dust off a surface and can leave circular or arcuate scratches in soft rocks. DRT scratching is not a rigorous test of a rock hardness because there is a small amount of uncertainty in the vertical placement of the DRT above the surface, as well as its approach angle to the target. These small uncertainties lead to target-to-target variability in how firmly the DRT brushes press against the surface, although hinges on the brushes are designed to buffer some of this uncertainty. Testing on the DRT flight model shows that the force applied to a surface by the DRT remains relatively constant even when the DRT is used at a variety of distances from the surface (Davis et al., 2012).

For our exploration, we compared the variability in rock response to dust removal. Consider the behavior of a relatively soft target. If the DRT is firmly pressed down on the surface, it will scratch the target as it removes the dust. However, if the DRT is just barely pressing on the surface, it will remove the dust but have less potential to leave scratches. Thus, if a target exhibits scratches, we interpret the target to be less lithified (i.e., a "soft" target). If a single target does not exhibit scratches, the target cannot *a priori* be presumed to be more lithified (i.e., a "hard" target), but if multiple similar lithologies all lack scratches, we can be more confident in assessing relative hardness. An assessment of the relative hardness of VRR drill targets (determined by whether the drill was successful or incomplete) is consistent with the hardness results from the DRT "scratch test" (see supporting information S2 for additional details). For all DRT targets, we evaluate whether there are deep, shallow, or no scratches (Table 1 and Figure 6). Many targets on VRR exhibit no scratches, which indicates that VRR rocks are generally very hard.

3.2.3. Grain Size

Gini index mean score results from 161 rocks suggest that VRR is dominated (75%) by rocks with mud-sized grains (Figure 7). We interpret these rocks, as did Edgar et al. (2020), as mudstones. Intervals with coarse silt to very fine sand were also detected, indicating the presence of siltstone and possibly fine-grained sandstone. Because the Gini index mean score is sensitive to compositional variation, it is also possible that

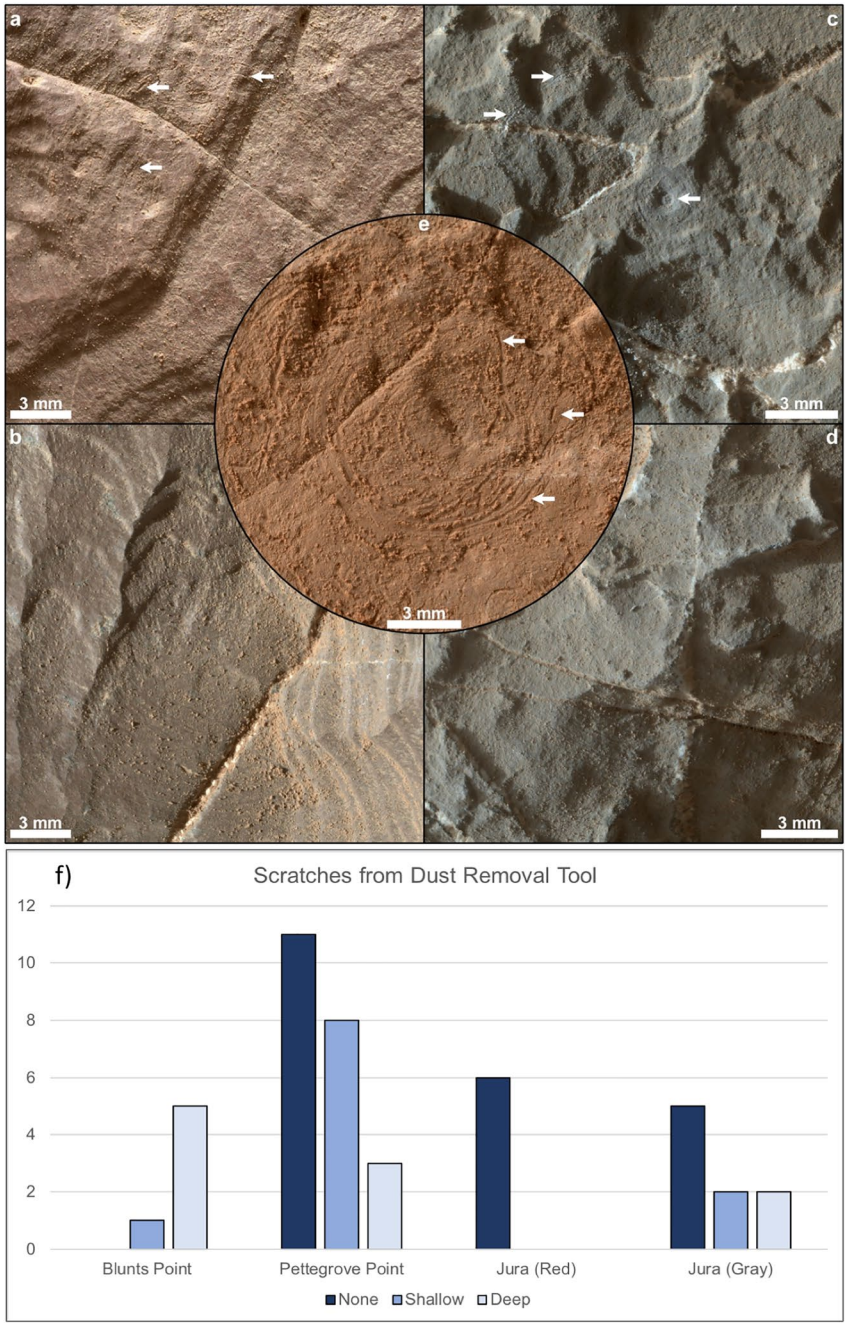


Figure 6. (a–e) Post-DRT MAHLI images. Arrows point to scratches left by the DRT. (a) Example from Pettegrove Point member showing shallow scratches in the Mitten Ledge target. (b) Example from the red Jura member showing no scratches in Drakensberg. (c) Example from the gray Jura member showing deep scratches in Ross of Mull. (d) Another example from the gray Jura member showing no scratches in Newmachar. (e) Example from the Blunts Point member showing deep scratches in Floodwood. (f) Chart showing the distribution of DRT scratches organized by member. DRT, Dust Removal Tool; MAHLI, Mars Hand Lens Imager.

the higher Gini indexes result from compositional contributions from nonresolvable diagenetic features and not from differences in grain size. Differentiating between heterogeneities resulting from diagenetic contributions and differences in grain size may be difficult when both are not resolvable in image data (Rivera-Hernández et al., 2020). However, several targets in the Jura member that are estimated to be siltstones or very fine sandstones by the Gini index mean score exhibit granular textures and contain coarse silt to

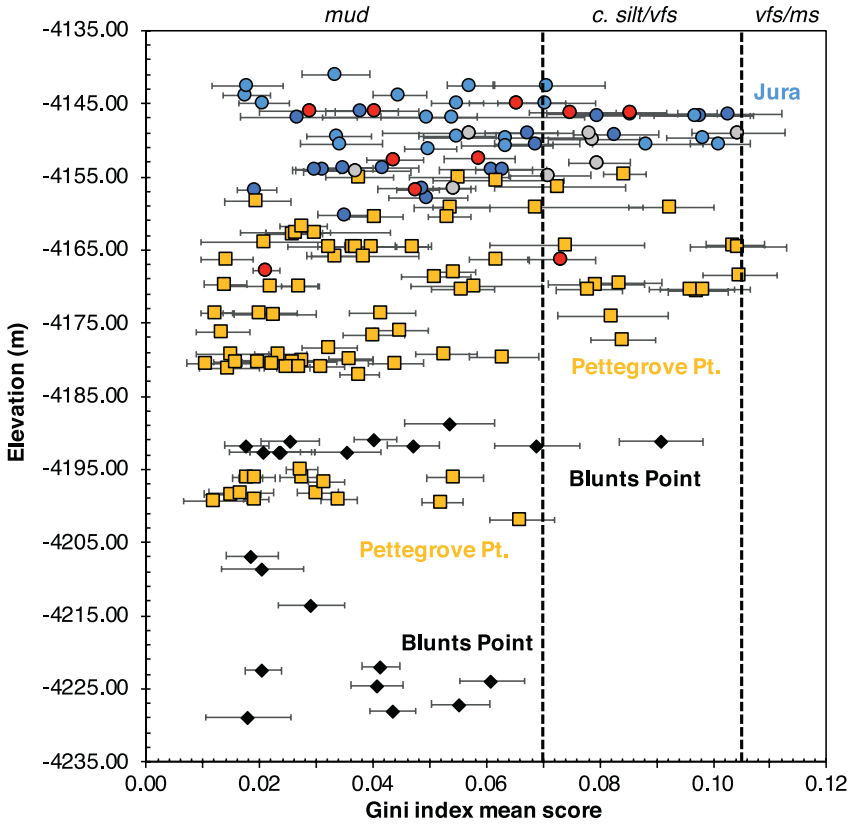


Figure 7. Gini index mean score results plotted against target elevation. Black diamonds represent targets in the Blunts Point member, yellow squares are targets within the Pettegrove Point member, and circles are targets within the Jura member—where the red or gray color of the circles corresponds to the host rock color (i.e., red circles are red Jura targets) and blue circles correspond to targets with unknown color due to lack of MAHLI coverage. The vertical lines denote the transition between grain size ranges; c. silt is coarse silt, vfs is very fine sand, and ms is medium sand. Rivera-Hernández (2020a, 2020b) reports the numerical data used to create this figure.

very fine sand grains that are able to be resolved in MAHLI images, which supports the Gini index grain size classification.

Table 2 records the Gini index grain size classification for targets of different colors. To compare grain size estimates with the amount diagenetic features that are present in a target, we obtained an average number of diagenetic features present in each target (Table 3). We first find the sum of diagenetic features (the fine-scale features outlined in Section 4.1 except for continuous laminations) identified in each target. For example, a target that has mixed tone crystal features and dark gray vein-associated features would receive a score of 2. Then these scores are averaged to get the average number of diagenetic features that are present in targets of specific estimated grain size classification.

Table 2
G_{MEAN} Results in the Jura Only for Targets With Both ChemCam and MAHLI Coverage Such That a Target Color Could be Defined

Color	Total number of targets	Mean G_{MEAN}	Mean Gini grain size
Red Jura	10	0.05 ± 0.02	Mud
Gray Jura	8	0.07 ± 0.02	Mud to coarse silt/very fine sand

4. Observed Distribution of Features

4.1. Distribution of Features Within Stratigraphic Members

The results of our examination of fine-scale features are organized by stratigraphic member in Figure 8. Here, we discuss each stratigraphic member's characteristics as determined by the presence of fine-scale depositional and diagenetic features. Figure 9 shows representative MAHLI targets from each of the members, and Tables 2 and 3 summarize grain sizes and distributions of diagenetic features.

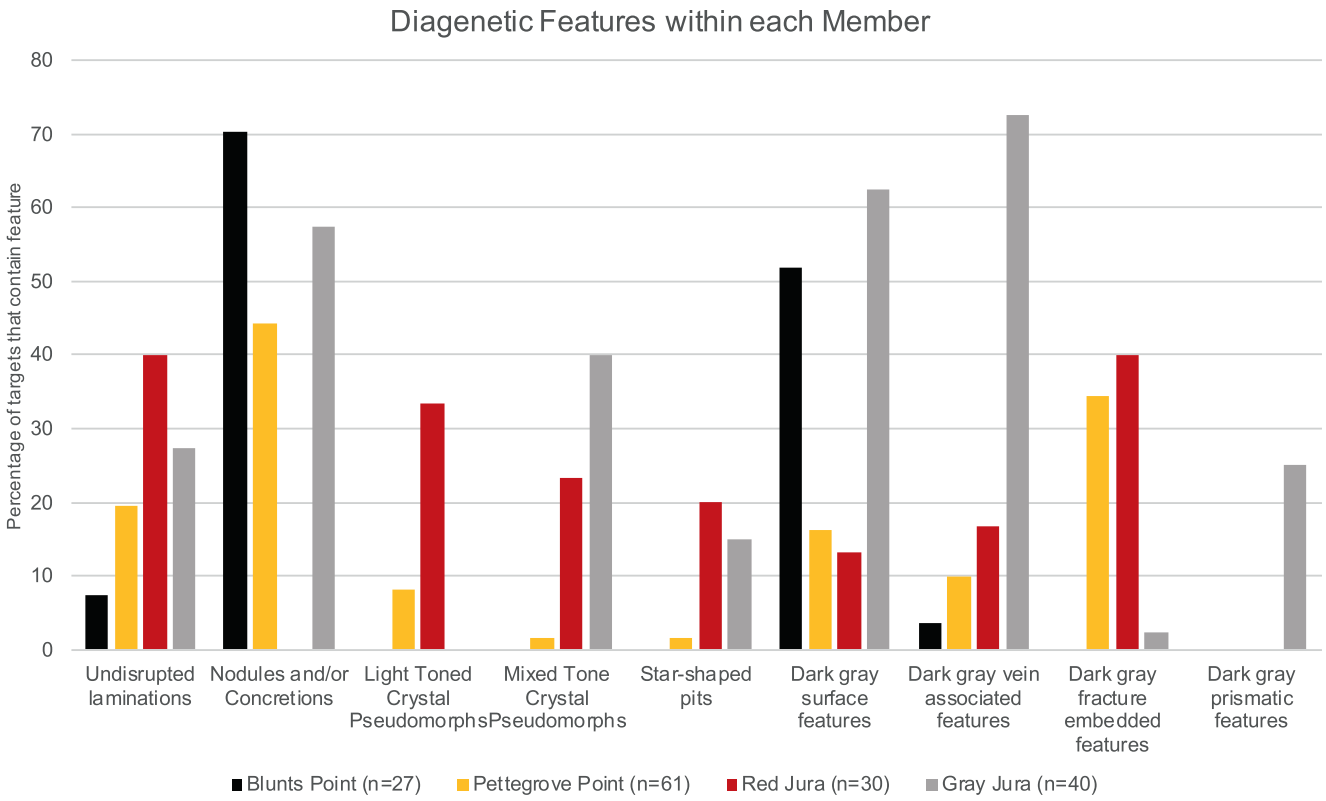


Figure 8. Survey of fine-scale features organized by the stratigraphic member and reported as a percentage of the total number of targets for each member (i.e., in the Red Jura, 12 out of 30 targets exhibited uninterrupted, continuous laminations, reported as 40%). Data are also reported in Table S1.

4.1.1. Blunts Point

Although only a subset of targets from Blunts Point is included in this study, these rocks are defined by a large number of resistant veins that stand out from the relatively recessive host rock (Figure 5a; Edgar et al., 2020). The majority of DRT targets in Blunts Point also exhibit deep scratches (i.e., Floodwood in Figure 6e), which supports an interpretation of relatively poorly cemented bedrock. Numerous veins that crosscut the primary bedding readily obscure bedding features, which is why only 7% of targets exhibited continuous lamination. Blunts Point targets exhibit a grain size estimate consistent with mudstone deposition, and the host rock in the Blunts Point member is generally red in color, with no examples of gray host rock. The most prevalent diagenetic features within Blunts Point strata are nodules (70% of the targets) and dark-toned surface features (52% of targets); no crystal features or potential crystal molds were observed. Dark gray features were generally rare, with the exception of dark-toned surfaces and one dark gray vein-associated feature (target Burnt Coat).

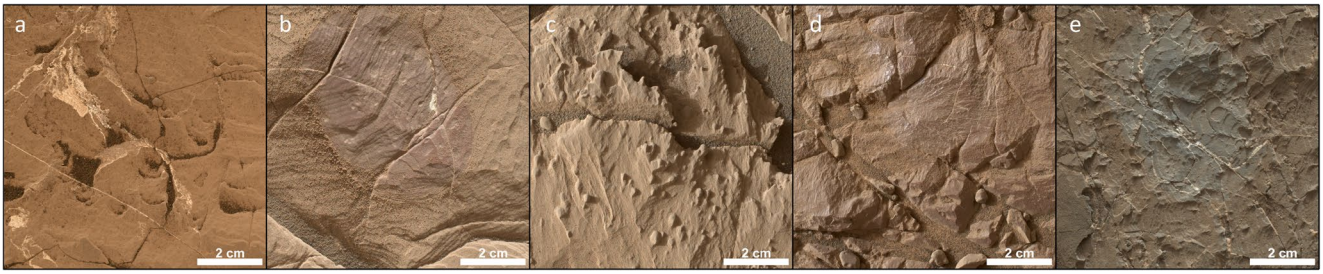


Figure 9. MAHLI targets representative of each stratigraphic member. (a) Blunts Point, McFarland Mountain. (b) Pettegrove Point with laminae, Mitten Ledge. (c) Pettegrove Point with nodules, Troll Valley. (d) Red Jura, Woodhill. (e) Gray Jura, Unst. MAHLI, Mars Hand Lens Imager.

Table 3
Comparing Gini Index Mean Score Grain Size Classification, the Occurrence of Gray Targets, and the Number of Types of Diagenetic Features for Targets That Had Both ChemCam and MAHLI Coverage

Gini grain size classification	Number of targets within the grain size range	Percent of targets that are gray (determined by MAHLI) (%)	Average number of diagenetic features present in each target (from Table 1)
Mud	30	10	1.33
Mud to coarse silt/very fine sand	4	25	1.75
Coarse silt/very fine sand	9	44	2.4

4.1.2. Pettegrove Point

Pettegrove Point targets generally have two distinct appearances: exhibiting either continuous lamination (Figure 9b) or a high concentration of nodules that obscure lamination (Figure 9c). Bedrock ranges from tan to red to purple, with red colors being the most common, although there are two gray Pettegrove Point targets. DRT targets in Pettegrove Point range from exhibiting no scratches to deep scratches (Figure 6a shows shallow scratches in the target Mitten Ledge). Light-toned veins in Pettegrove Point are also recessive relative to the host rock (Figure 5b). These observations indicate that Pettegrove Point member rocks are likely harder, or better cemented, than Blunts Point member rocks. The average estimated grain size of Pettegrove Point targets is within the range of mudstones, but the grain size of individual targets shows a range up to very fine sand to medium size sand (Figure 7). Neither of the gray Pettegrove Point targets were targeted by ChemCam in order to assess the Gini index, preventing grain size estimates for these targets. Crystal features (both light and mixed toned) and crystal molds are rare. Some dark gray features are observed in Pettegrove Point, including dark gray surface features and dark gray vein-associated features.

4.1.3. Jura

Two distinct categories of targets within the Jura member are red and gray (as seen in MAHLI images). The differences in fine-scale features within these two categories warrant separate discussions.

4.1.3.1. Red Jura

Red Jura targets occur as highly fractured and poorly exposed bedrock regions; therefore, few areally extensive outcrops of red Jura material were targeted by MAHLI. Although nodules are fairly common within our study area (44% of all targets), red Jura targets are unique in that they show no nodules. The highest concentration of continuous lamination occurred in red Jura targets (40% of targets), which may reflect the lack of nodules or other lamina-disrupting features. Scratches are absent from red Jura DRT targets (Figure 6). Similar to the underlying Pettegrove Point member, veins in red Jura material are recessive as relative to the host rock. These observations indicate that rocks of the red Jura member are likely harder (i.e., more heavily cemented) than rocks in the Blunts Point member. Grain size estimates for red Jura targets suggest that they are, on average, mudstone, but two targets are estimated to have grain sizes that are the boundary of mud to coarse silt/very fine sand range and one target is estimated to have coarse silt to very fine sand size grains. Both light-toned and mixed-toned crystal features occur in red Jura targets, as well as star-shaped pits inferred to represent crystal molds. A small fraction of red Jura targets has dark-toned surface features (13%) and dark-toned vein-associated features (17%).

4.1.3.2. Gray Jura

Gray Jura targets are characterized by a distinct gray color and the presence of numerous submm-to-cm scale diagenetic features. Dark gray features are especially abundant in gray Jura targets (85% of gray Jura targets exhibit at least one dark gray feature). Dark gray prismatic features only occur in gray Jura targets. Dark gray surface features and dark gray vein-associated features occur extensively (63% and 73%, respectively), but dark gray fracture-embedded features are rare (3%). There are many instances of crystal features within gray Jura targets (40%). These occurrences show mixed tone crystal pseudomorphs; no light-toned crystal pseudomorphs are observed. Most gray Jura targets do not exhibit scratches from the DRT, although some targets show scratches (Figure 6). Similar to Pettegrove Point and red Jura members, veins in gray Jura material are recessive relative to the host rock (Figure 5c). These observations indicate that rocks in the gray Jura member (as with the Pettegrove Point and red Jura members) are relatively harder than rocks in the Blunts Point member. Gray Jura targets exhibit a slightly larger average G_{MEAN} grain size value compared to the red Jura, although the two values are within the error estimates (Table 2).

5. Diagenesis on VRR

All of the features identified and analyzed in this paper (except fine-scale laminations and grain size variations) are interpreted to result from postdepositional diagenesis. Here, we discuss our interpretations related to the relationship between primary and secondary features, iron mobility during diagenesis, and the implications for the topographic relief of VRR.

5.1. Relationship Between Primary and Secondary Features

5.1.1. Grain Size vs. Diagenetic Indicators

The average estimated grain size of all stratigraphic members is similar, which supports an interpretation that these sediments were all deposited in similar, lacustrine environments (Edgar et al., 2020). However, we propose that the observed slight variations in grain size may have played a primary role in contributing to differences in diagenetic expression.

When examining the different members together (Table 3), we find a correlation between the G_{MEAN} value and the number of different types of diagenetic features that are present in a target. Targets estimated to have coarser grains tend to exhibit a greater number of distinct types of diagenetic feature (Table 3). Additionally, gray Jura targets are more likely to have coarser estimated grain size ranges (Figure 7 and Table 2). These results suggest that subtle differences in grain size on VRR resulted in a differing expression of diagenesis. This phenomenon is well documented on Earth (Houseknecht, 1984; James et al., 1986; Porter & James, 1986; Putnis & Mauthe, 2001). Coarser-grained rocks (such as sandstones) are commonly more permeable than finer-grained rocks, so fluids will preferentially travel through coarser-grained intervals within a stratigraphic package. Our results show that gray Jura rocks contain the most diagenetic features, and we interpret the color difference of this unit—which represents a distinct departure from dominantly red-colored rocks within the succession—to also result from diagenesis. Our interpretation is consistent with subtle differences in grain sizes influencing diagenesis; the same event that resulted in the diagenetic features discussed above also could have caused the gray color of the rocks.

In this scenario, we assume that larger grains are associated with greater porosity (i.e., larger pore spaces) between individual grains. Although differences in grain size are not uniquely linked to permeability, which describes the pathway of fluid movement between pore spaces, greater pore space is frequently associated with greater permeability (Beard & Weyl, 1973; Chilingar, 1964). Additionally, the hypothesis that Gale crater might have once been completely filled with sediment (e.g., Edgett et al., 2020; Malin & Edgett, 2000) implies that the exposed strata observed by the rover was buried by at least several kilometers of overburden. Under these conditions, we would expect that strata composed of differing grain size would have behaved differently during compaction. Whereas compaction would be expected to reduce porosity in all components, permeability tends to be reduced more in finer-grained size rocks (Wang et al., 2017) so strata containing larger grain sizes are expected to retain higher overall porosity. This could result in coarse-grained intervals retaining a greater relative porosity and permeability as compared to fine-grained intervals, which is consistent with observations of diagenetic variability in these strata. If these strata contained soluble phases (such as sulfate), water-rock interaction may have additionally resulted in dissolution of these phases and a diagenetic increase in both porosity and permeability, leading to even greater potential for water-rock interaction, potentially recorded here by the recrystallization of hematite phases.

5.1.2. Member Boundaries vs. Diagenetic Features

Overall, the diagenetic features present in the Blunts Point member are distinct from those in the Pettegrove Point and Jura members. Targets within Blunts Point have few dark gray diagenetic features and no crystal pseudomorphs and are not as well cemented as the targets in Pettegrove Point or Jura. This indicates that the Blunts Point member experienced a different diagenetic history than the rocks in VRR.

While the stratigraphic members of VRR (Pettegrove Point and Jura) are distinct in terms of both the number and variety of diagenetic features that are present (Figure 8), we conclude that, in general, diagenetic features are not constrained by member boundaries within VRR. First, while crystal features are more abundant in Jura targets, they also occur in Pettegrove Point targets. Next, gray targets and dark gray diagenetic

features were observed in both Pettegrove Point and Jura targets. Also, the most considerable differences in diagenetic features on VRR occur in relationship to rock color. The Jura member exhibits both red and gray rocks, and the number of different diagenetic features (especially dark gray features) varies between red and gray Jura targets. Together, these observations indicate that while the primary lithology (i.e., grain size) influences the types of diagenesis that occurred within VRR targets, specific diagenetic events were not significantly restricted by member boundaries within VRR.

5.2. Diagenetic Features and Iron Mobility

Most prominent among diagenetic features in the VRR succession are dark gray features that have been shown to be iron-rich (L'Haridon et al., 2020). L'Haridon et al. (2020) also note that many dark gray features exhibit light-toned halos in the host rock that are depleted in iron content. Such features occur most prominently within gray-colored host rock. These alteration halos suggest that the iron from a very local area of the host rock was reduced, mobilized, and recrystallized as the dark gray diagenetic features. Although we only identify light-toned halos in two MAHLI images (targets Canna and Portobello, Table 1), the lack of alteration halos in MAHLI images could also reflect the different wavelengths of the two cameras. ChemCam's Remote Micro-Imager is panchromatic, measuring light from 240 to 900 nm (Le Mouelic et al., 2015), whereas MAHLI's wavelength range is 365–670 nm (Edgett et al., 2012). ChemCam's broader wavelength range could be related to why alteration halos are observed in that data set and not in MAHLI images.

Even without considering the iron-depleted alteration halos, there are variations in the iron content within VRR: the dark gray diagenetic features have a higher iron content than the host rock (L'Haridon et al., 2020; Rampe et al., 2020). Here, we discuss iron mobility on VRR and how the dark gray diagenetic features formed. We also consider whether the color variability on VRR (red vs. gray) is related to iron mobility. Results from the CheMin instrument show that the amount of iron-bearing minerals in VRR drill targets (representing the host rock) varies within a narrow range of ~10–~17% (Rampe et al., 2020). Additionally, results from Mastcam multispectral data suggest that the degree of hematite crystallization is variable at VRR (Horgan et al., 2020). Horgan et al. (2020) specifically propose that hematite may have become coarser in some locations of VRR during diagenetic recrystallization. Because fine-grained hematite is red, while coarser-grained hematite is gray, recrystallization of hematite may be reflected in the gray host rock on VRR (Horgan et al., 2020). Recrystallization of hematite into coarser grains is not expected to have any impact on the estimates of detrital grain size in host materials, as this color change occurs at around 3–5 μm in lab samples (Morris et al., 2020), which is an order of magnitude smaller than the finest siliciclastic grains resolvable by MAHLI (62.5 μm). These observations suggest that the gray rocks on VRR reflect a widespread region of diagenetic recrystallization in which iron within the bedrock was both remobilized (into specific diagenetic features) and recrystallized (within the matrix).

To address whether iron within diagenetic features could feasibly be sourced from VRR bedrock, we used an MAHLI image to estimate the volume of dark gray diagenetic features as compared to the host rock volume to calculate whether the total amount of hematite in this area was consistent with the expected bulk hematite value (see supporting information S3). For example, iron oxide concretions in sandstone outcrops in Utah must have been precipitated from advective flow that supplied the iron because the host rock alone contained insufficient amounts of iron (Chan et al., 2005; Yoshida et al., 2018). We find that the VRR host rock could supply the amount of iron required to create the dark gray diagenetic features (supporting information S3). We propose that the dark-gray iron-rich diagenetic features were plausibly sourced from the VRR bedrock and that advective flow of an outside iron-rich fluid is not necessary.

Although the gray Jura member contains the most abundant and widespread dark gray diagenetic features, we also identify dark gray features in other members of VRR. We speculate that the dark gray features in red Jura and in Pettegrove Point members were also sourced from iron mobilized during extensive fluid flow through the gray VRR rocks. The majority of gray targets (all but two in this data set) occurred in the gray Jura member, so we use our results analyzing diagenetic features that occur in each stratigraphic member (Section 5) to investigate iron mobility between members. The abundance of dark gray vein-associated features, for instance, decreases with stratigraphic distance from gray Jura rocks (73% of gray Jura, 17% of red Jura targets, 10% of Pettegrove Point targets, and 4% of Blunts Point targets), which supports the

hypothesis that the gray Jura host rock may have provided the iron source for the dark-toned features. We propose that the fluids that interacted with the gray Jura sediment were generally unable to permeate the red Jura sediment, so the fluids traveled through fractures, precipitating dark gray vein-associated features. Decreased permeability of red Jura sediment is supported by the general absence of nodules and the close association of diagenetic features with local fractures. As the fluids traveled farther along the fractures into Pettegrove Point and Blunts Point, iron-rich minerals continued to precipitate but at a decreased frequency. Blunts Point, the farthest member studied here, generally exhibits the fewest dark gray features. Given the occurrence of a limited amount of gray rocks in the Pettegrove Point member, we hypothesize that these rocks also experienced iron mobilization and hematite recrystallization but it was less extensive than in the gray Jura member rocks.

5.3. Why is VRR a Ridge?

Our results provide evidence that VRR represents a localized region of better cemented, or harder, bedrock resulting from localized diagenesis. Rocks from both the Pettegrove Point and Jura members are hard, as demonstrated by the vein morphology on the ridge as well as the lack of DRT scratches in red Jura (Figure 6) and the unsuccessful drill attempts in both Pettegrove Point and gray Jura (Table S2). Similarity in average grain size between the stratigraphic members investigated here indicates that the hardness of VRR rocks cannot be attributed only to grain size or stratigraphic member. Rather, our data indicate that rock hardness is more directly related to the degree of postdepositional diagenesis. Our interpretation that VRR rocks are hard due to diagenesis is consistent with inferences from other studies, including Jacob et al. (2020) who suggested that primary cementation may have resulted in the relative hardness of VRR rocks and Fraeman et al. (2020) who suggested that the relative erosional resistance in this region may be related to recrystallization by groundwater. Interestingly, the topographic expression of the VRR is spatially associated with the presence of overlying strata associated with the Greenheugh pediment and associated fan deposits deriving from a major unconformity that may postdate the Mt. Sharp sedimentary succession (Fraeman et al., 2020). This spatial co-occurrence permits speculation that the main diagenetic features and iron remobilization within the VRR recorded here could even be related to postdeposition, postburial, and postexhumation fluid flow related to the unconformity.

6. Timeline and Broader Implications for Diagenesis at VRR

6.1. Using Fine-Scale Features to Place Constraints on a Timeline of Diagenetic Activity

Finally, we can use the results of this study to place constraints on the relative timing of the diagenetic events that impacted VRR (Figure 10).

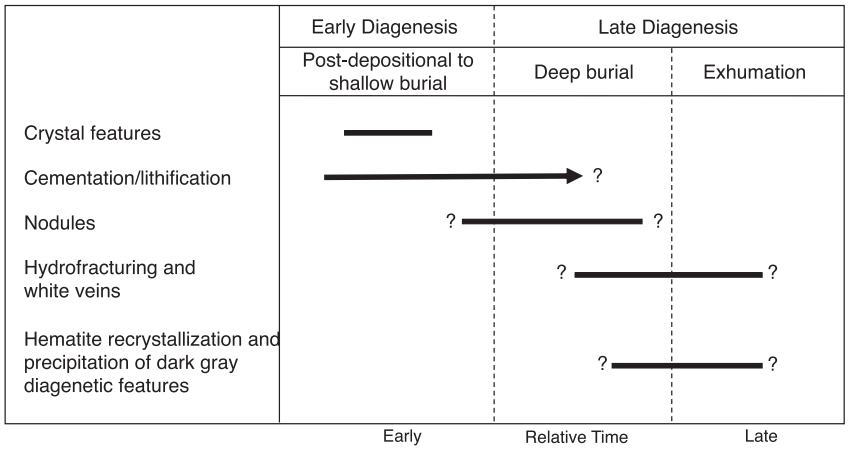


Figure 10. Relative timing of diagenetic events and formation of diagenetic features.

We hypothesize that the primary crystal features precipitated during early diagenesis. The crystals must have formed after deposition and initial lithification and cementation because the primary laminations are not clearly disrupted or deformed. However, the crystals also must have formed during early diagenesis because they occur in both red and gray Jura rocks, and red Jura became relatively impermeable at some point during diagenesis.

We hypothesize that lithification (including cementation and compaction) started during early diagenesis and continued through at least early burial. Compared to previously studied strata in the Murray formation, VRR is unique in its hardness and erosional resistance. A combination of enhanced cementation, diagenetic recrystallization, and grain coarsening of iron-rich cements appears to have further enhanced erosional resistance of these units. Although cementation would have begun in early diagenesis, before the crystal features were precipitated, it appears to have continued into burial realms. Hydrofracture of VRR stratigraphy would have occurred, as well, under burial conditions, although (1) hydrofractures may have occurred at multiple times during the geologic history of these samples (Kronyak et al., 2019) and (2) the filling of hydrofractures with minerals may have occurred either during the initial hydrofracture event, or later either in the burial realm, or even during exhumation (Kronyak et al., 2019). Association of hydrofracture veins with dark gray diagenetic fracture-associated features suggests that these features represent one of the latest stages of diagenetic recrystallization, occurring either during burial or exhumation.

Firm constraints regarding the timing of the nodule-forming event(s) are not identifiable from this study on VRR. Relative to other features, nodules formed after at least early lithification but before the white veins because veins crosscut nodules in several locations (targets Barberton and Newmacher, see Figure S2). Veins crosscutting nodules have been observed in Gale crater previously (Grotzinger et al., 2014; Nachon et al., 2014; Vaniman et al., 2014). Additionally, Sun et al. (2019) investigated all nodules along *Curiosity*'s traverse and determined that the nodules on VRR were smaller than nodules in other parts of the Murray formation due to the increased lithification and cementation in the ridge, which indicates the nodules formed during at an intermediate stage of diagenesis, after initial lithification, but prior to hydrofracture in the deep burial realm.

We hypothesize that the fluid event(s) that facilitated iron mobility on VRR occurred during late diagenesis, although we cannot clearly identify whether this occurred during deep burial or upon exhumation of these strata. If the crystal pseudomorphs were replaced by hematite during deep burial, we might expect to see deformation of the crystal shapes resulting from the overburden pressure. The absence of pseudomorph deformation could suggest that diagenetic recrystallization may have occurred during exhumation, after the main permeability of the Jura member was reduced, and when overburden pressure was reduced.

6.2. Broader Implications

The abundance and widespread occurrence of submillimeter-to-centimeter scale diagenetic features in VRR emphasize the extent and importance of secondary alteration in the Murray formation and illustrate that water-rock interactions occurred in Gale crater even after deposition and lithification. These results provide additional evidence that liquid water was present on Mars—at least episodically—for a period of time that spans the full lifetime of Gale crater, from the initial deposition of sediment, through burial, and into exhumation.

These results are also consistent with the hypothesis that Gale crater experienced a range of environmental conditions early in its history. The presence of long-lived lacustrine environments—indicated by the total thickness of Murray formation rocks—suggests long periods of time where wet conditions prevailed, at least episodically (Edgar et al., 2020). Precipitation of gypsum crystals in VRR rocks, and elsewhere in the Murray formation (Kah et al., 2018), during early diagenesis suggests at least episodic periods of aridity experienced by the Murray formation lake (see also Stein et al., 2018). Alternatively, gypsum within VRR may be associated with more regional shifts in climate associated with deposition of a prominent sulfate-bearing unit that overlies the VRR stratigraphy (Milliken et al., 2010). Constraining the timing and understanding the nature of the shift from wet conditions to more arid conditions is crucial for learning more about habitability on early Mars. Characterizing this change in environment will help constrain how long aqueous and potentially habitable conditions persisted on Mars and enable us to learn more about how the change to an arid environment occurred.

7. Summary and Conclusions

In sum, we find that submillimeter-to-centimeter scale diagenetic features are present throughout VRR and demonstrate intensive postdepositional alteration and occurrence of water-rock interaction. Although diagenetic fluid activity is not uniquely constrained to specific sedimentary members, grain size variation within these members appears to have played a critical role in the distribution of diagenetic features, wherein coarser grain sizes correspond to more diagenetic features. Diagenetic features are most prevalent and varied in the gray Jura member. In these rocks, dark-gray iron-rich diagenetic features are commonly associated with fractures and veins in the bedrock; such diagenesis extended downward into the red Jura, and to a lesser degree, the underlying Pettegrove Point, suggesting that iron-rich fluids were likely sourced from the gray Jura rocks during a diagenetic event that caused dissolution and recrystallization of the iron in the host rock. Constraints on the timing of diagenetic evens indicate a long history of fluid-rock interaction in Gale crater, which spans from deposition, through burial, and ultimately through exhumation of the Murray formation sedimentary package.

Data Availability Statement

All data used in this study are publicly available on the Planetary Data System either in the MAHLI archive on the PDS Imaging Node or in the ChemCam archive (https://pds-geosciences.wustl.edu/missions/msl/). The results from analyzing MAHLI images (shown in Table 1) can also be accessed via Mendeley Data (https://doi.org/10.17632/mksd84gsz8.1). Data used to estimate grain size using the Gini index mean score technique can be accessed via Zenodo: https://doi.org/10.5281/zenodo.3605603 (sols 766–1804) and https://doi.org/10.5281/zenodo.3672073 (1808–2298).

Acknowledgments
This research was partially supported by the NASA Mars Science Laboratory Participating Scientist Program (PI: Edwards). Additionally, a portion of this research was carried out at the Jet Propulsion Laboratory, California Institute of Technology, under a contract with the National Aeronautics and Space Administration. Additionally, we thank Peter Mozley and two anonymous reviewers for their helpful comments. Any use of trade, firm, or product names is for descriptive purposes only and does not imply endorsement by the U.S. Government.

References

Anderson, R., & Bell, J. F. (2010). Geologic mapping and characterization of Gale crater and implications for its potential as a Mars Science Laboratory landing site. *Mars*, *5*, 76–128. https://doi.org/10.1555/mars.2010.0004

Andeskie, A. S., Benison, K. C., Eichenlaub, L. A., & Raine, R. (2018). Acid-saline-lake systems of the Triassic Mercia Mudstone Group, County Antrim, Northern Ireland. *Journal of Sedimentary Research*, *88*(3), 385–398. https://doi.org/10.2110/jsr.2018.14

Beard, D. C., & Weyl, P. K. (1973). Influence of texture on porosity and permeability of unconsolidated sand. *AAPG Bulletin*, *57*(2), 349–369. https://doi.org/10.1306/819A4272-16C5-11D7-8645000102C1865D

Beitler, B., Parry, W. T., & Chan, M. A. (2005). Fingerprints of fluid flow: Chemical diagenetic history of the Jurassic Navajo Sandstone, southern Utah, U.S.A. *Journal of Sedimentary Research*, *75*(4), 547–561. https://doi.org/10.2110/jsr.2005.045

Bell, J., Malin, M. C., Caplinger, M. A., Fahle, J., Wolff, J., Cantor, B. A., et al. (2013). Calibration and performance of the Mars Reconnaissance Orbiter context camera (CTX) (Vol. *8*, pp. 14). https://doi.org/10.1555/mars.2013.0001

Bennett, K. (2021). Diagenetic features observed within Vera Rubin ridge, Gale crater, Mars (Version 1) [Dataset]. Mendeley Data. https://doi.org/10.17632/mksd84gsz8.1

Bennett, K. A., Hill, J. R., Murray, K. C., Edwards, C. S., Bell, J. F., & Christensen, P. R. (2018). THEMIS-VIS investigations of sand at Gale crater. *Earth and Space Science*, *5*, 352–363. https://doi.org/10.1029/2018EA000380

Caswell, T. E., & Milliken, R. E. (2017). Evidence for hydraulic fracturing at Gale crater, Mars: Implications for burial depth of the Yellowknife Bay formation. *Earth and Planetary Science Letters*, *468*, 72–84. https://doi.org/10.1016/j.epsl.2017.03.033

Chan, M. A., Bowen, B. B., & Parry, W. T. (2005). Red rock and red planet diagenesis: Comparisons of Earth and Mars concretions. *GSA Today*, *15*(8), https://doi.org/10.1130/1052-5173(2005)015<4:RRARPD>2.0.CO;2

Chan, M. A., Parry, W. T., & Bowman, J. R. (2000). Diagenetic hematite and manganese oxides and fault-related fluid flow in Jurassic sandstones, southeastern Utah. *AAPG Bulletin*, *84*(9), 1281–1310. https://doi.org/10.1306/A9673E82-1738-11D7-8645000102C1865D

Chilingar, G. V. (1964). Relationship between porosity, permeability, and grain-size distribution of sands and sandstones. In L. M. J. U. van Straaten (Ed.), Developments in sedimentology (Vol. 1, pp. 71–75). Amsterdam, Netherlands: Elsevier. https://doi.org/10.1016/S0070-4571(08)70469-2

Cousin, A., Dehouck, E., Meslin, P.-Y., Forni, O., Williams, A. J., Stein, N., et al. (2017). Geochemistry of the bagnold dune field as observed by ChemCam and comparison with other aeolian deposits at gale crater. *Journal of Geophysical Research: Planets*, *122*, 2144–2162. https://doi.org/10.1002/2017JE005261

Davis, K., Herman, J., Maksymuk, M., Wilson, J., Chu, P., Burke, K., et al. (2012). Mars science laboratory's dust removal tool. *Proceedings of the Aerospace Mechanisms Symposium.*

Edgar, L. A., Fedo, C. M., Gupta, S., Banham, S. G., Fraeman, A. A., Grotzinger, J. P., et al. (2020). A lacustrine paleoenvironment recorded at Vera Rubin ridge, gale crater: Overview of the sedimentology and stratigraphy observed by the Mars Science Laboratory Curiosity Rover. *Journal of Geophysical Research: Planets*, *125*, e2019JE006307. https://doi.org/10.1029/2019JE006307

Edgett, K. (2013a). MSL Mars Hand Lens Imager Camera RDR IMAGE V1.0. NASA Planetary Data System. https://www.doi.org/10.17189/1520292

Edgett, K. (2013b). MSL Mars Hand Lens Imager Camera RDR ZSTACK V1.0. NASA Planetary Data System. https://www.doi.org/10.17189/1520169

Edgett, K., Caplinger, M., Maki, J., Ravine, M., Ghaemi, F., McNair, S., et al. (2015). Curiosity's robotic arm-mounted Mars Hand Lens Imager (MAHLI): Characterization and calibration status (Technical Report). https://doi.org/10.13140/RG.2.1.3798.5447

Edgett, K. S., Banham, S. G., Bennett, K. A., Edgar, L. A., Edwards, C. S., Fairén, A. G., et al. (2020). Extraformational sediment recycling on Mars. *Geosphere*, *16*(6), 1508–1537. https://doi.org/10.1130/GES02244.1

Edgett, K. S., Yingst, R. A., Ravine, M. A., Caplinger, M. A., Maki, J. N., Ghaemi, F. T., et al. (2012). Curiosity's Mars Hand Lens Imager (MAHLI) Investigation. *Space Science Reviews*, *170*(1–4), 259–317. https://doi.org/10.1007/s11214-012-9910-4

Fraeman, A. A., Arvidson, R. E., Catalano, J. G., Grotzinger, J. P., Morris, R. V., Murchie, S. L., et al. (2013). A hematite-bearing layer in Gale crater, Mars: Mapping and implications for past aqueous conditions. *Geology*, *41*(10), 1103–1106. https://doi.org/10.1130/G34613.1

Fraeman, A. A., Edgar, L. A., Rampe, E. B., Thompson, L. M., Frydenvang, J., Fedo, C. M., et al. (2020). Evidence for a diagenetic origin of Vera Rubin ridge, Gale crater, Mars: Summary and synthesis of Curiosity's exploration campaign. *Journal of Geophysical Research: Planets*, *125*, e2020JE006527. https://doi.org/10.1029/2020JE006527

Frydenvang, J., Gasda, P. J., Hurowitz, J. A., Grotzinger, J. P., Wiens, R. C., Newsom, H. E., et al. (2017). Diagenetic silica enrichment and late-stage groundwater activity in Gale crater, Mars. *Geophysical Research Letters*, *44*, 4716–4724. https://doi.org/10.1002/2017GL073323

Grotzinger, J. P., Gupta, S., Malin, M. C., Rubin, D. M., Schieber, J., Siebach, K., et al. (2015). Deposition, exhumation, and paleoclimate of an ancient lake deposit, Gale crater, Mars. *Science*, *350*(6257), aac7575. https://doi.org/10.1126/science.aac7575

Grotzinger, J. P., Sumner, D. Y., Kah, L. C., Stack, K., Gupta, S., Edgar, L., et al. (2014). A Habitable Fluvio-Lacustrine Environment at Yellowknife Bay, Gale Crater, Mars. *Science*, *343*(6169), 1242777. https://doi.org/10.1126/science.1242777

Guzewich, S. D., Lemmon, M., Smith, C. L., Martínez, G., Vicente-Retortillo, Á., Newman, C. E., et al. (2019). Mars science laboratory observations of the 2018/mars year 34 global dust storm. *Geophysical Research Letters*, *46*, 71–79. https://doi.org/10.1029/2018GL080839

Herkenhoff, K. E., Squyres, S. W., Bell, J. F., Maki, J. N., Arneson, H. M., Bertelsen, P., et al. (2003). Athena microscopic imager investigation. *Journal of Geophysical Research*, *108*(E12), 8065. https://doi.org/10.1029/2003JE002076

Horgan, B. H. N., Johnson, J. R., Fraeman, A. A., Rice, M. S., Seeger, C., Bell, J. F., et al. (2020). Diagenesis of Vera Rubin ridge, Gale crater, Mars, from Mastcam multispectral images. *Journal of Geophysical Research: Planets*, *125*, e2019JE006322. https://doi.org/10.1029/2019JE006322

Houseknecht, D. W. (1984). Influence of grain size and temperature on intergranular pressure solution, quartz cementation, and porosity in a quartzose sandstone. *Journal of Sedimentary Research*, *54*(2), 348–361. https://doi.org/10.1306/212F8418-2B24-11D7-8648000102C1865D

Jacob, S. R., Wellington, D. F., Bell, J. F., Achilles, C., Fraeman, A. A., Horgan, B., et al. (2020). Spectral, Compositional, and Physical Properties of the Upper Murray Formation and Vera Rubin Ridge, Gale Crater, Mars. *Journal of Geophysical Research: Planets*, *125*(11), e2019JE006290. https://doi.org/10.1029/2019JE006290

James, W. C., Wilmar, G. C., & Davidson, B. G. (1986). Role of quartz type and grain size in silica diagenesis, Nugget Sandstone, south-central Wyoming. *Journal of Sedimentary Research*, *56*(5), 657–662. https://doi.org/10.1306/212F8A03-2B24-11D7-8648000102C1865D

Kah, L. C., Stack, K. M., Eigenbrode, J. L., Yingst, R. A., & Edgett, K. S. (2018). Syndepositional precipitation of calcium sulfate in Gale crater, Mars. *Terra Nova*, *30*(6), 431–439. https://doi.org/10.1111/ter.12359

Kronyak, R. E., Arndt, C., Kah, L. C., & TerMaath, S. C. (2020). Predicting the mechanical and fracture properties of Mars analog sedimentary lithologies. *Earth and Space Science*, *7*, e2019EA000926. https://doi.org/10.1029/2019EA000926

Kronyak, R. E., Kah, L. C., Edgett, K. S., VanBommel, S. J., Thompson, L. M., Wiens, R. C., et al. (2019). Mineral-filled fractures as indicators of multigenerational fluid flow in the Pahrump Hills member of the Murray formation, Gale crater, Mars. *Earth and Space Science*, *6*, 238–265. https://doi.org/10.1029/2018EA000482

Le Mouélic, S., Gasnault, O., Herkenhoff, K. E., Bridges, N. T., Langevin, Y., Mangold, N., et al. (2015). The ChemCam Remote Micro-Imager at Gale crater: Review of the first year of operations on Mars. *Icarus*, *249*, 93–107. https://doi.org/10.1016/j.icarus.2014.05.030

L'Haridon, J., Mangold, N., Fraeman, A. A., Johnson, J. R., Cousin, A., Rapin, W., et al. (2020). Iron mobility during diagenesis at Vera Rubin ridge, Gale crater, Mars. *Journal of Geophysical Research: Planets*, *125*, e2019JE006299. https://doi.org/10.1029/2019JE006299

L'Haridon, J., Mangold, N., Meslin, P.-Y., Johnson, J. R., Rapin, W., Forni, O., et al. (2018). Chemical variability in mineralized veins observed by ChemCam on the lower slopes of Mount Sharp in Gale crater, Mars. *Icarus*, *311*, 69–86. https://doi.org/10.1016/j.icarus.2018.01.028

Loyd, S. J., & Corsetti, F. A. (2010). The origin of the millimeter-scale lamination in the neoproterozoic lower beck spring dolomite: Implications for widespread, fine-scale, layer-parallel diagenesis in precambrian carbonates. *Journal of Sedimentary Research*, *80*(7), 678–687. https://doi.org/10.2110/jsr.2010.063

Malin, M. C.& Edgett, K. S. (2000). Sedimentary rocks of early Mars. *Science*, *290*(5498), 1927–1937. https://doi.org/10.1126/science.290.5498.1927

Maurice, S., Wiens, R. C., Saccoccio, M., Barraclough, B., Gasnault, O., Forni, O., et al. (2012). The ChemCam instrument suite on the mars science laboratory (MSL) Rover: Science objectives and mast unit description. *Space Science Reviews*, *170*(1), 95–166. https://doi.org/10.1007/s11214-012-9912-2

McLennan, S. M., Bell, J. F., Calvin, W. M., Christensen, P. R., Clark, B. C., de Souza, P. A., et al. (2005). Provenance and diagenesis of the evaporite-bearing Burns formation, Meridiani Planum, Mars. *Earth and Planetary Science Letters*, *240*(1), 95–121. https://doi.org/10.1016/j.epsl.2005.09.041

Melezhik, V. A., Fallick, A. E., Rychanchik, D. V., & Kuznetsov, A. B. (2005). Palaeoproterozoic evaporites in Fennoscandia: Implications for seawater sulphate, the rise of atmospheric oxygen and local amplification of the δ13C excursion. *Terra Nova*, *17*(2), 141–148. https://doi.org/10.1111/j.1365-3121.2005.00600.x

Milliken, R. E., Grotzinger, J. P., & Thomson, B. J. (2010). Paleoclimate of Mars as captured by the stratigraphic record in Gale crater: Stratigraphy of gale crater. *Geophysical Research Letters*, *37*, L04201. https://doi.org/10.1029/2009GL041870

Minitti, M. E., Kah, L. C., Yingst, R. A., Edgett, K. S., Anderson, R. C., Beegle, L. W., et al. (2013). MAHLI at the Rocknest sand shadow: Science and science-enabling activities: MAHLI AT ROCKNEST. *Journal of Geophysical Research: Planets*, *118*(11), 2338–2360. https://doi.org/10.1002/2013JE004426

Minitti, M. E., Malin, M. C., Van Beek, J. K., Caplinger, M., Maki, J. N., Ravine, M., et al. (2019). Distribution of primary and secondary features in the Pahrump Hills outcrop (Gale crater, Mars) as seen in a Mars Descent Imager (MARDI) "sidewalk" mosaic. *Icarus*, *328*, 194–209. https://doi.org/10.1016/j.icarus.2019.03.005

Morris, R. V., Rampe, E. B., Vaniman, D. T., Christoffersen, R., Yen, A. S., Morrison, S. M., et al. (2020). Hydrothermal precipitation of sanidine (adularia) having full Al,Si structural disorder and specular hematite at Mauna Kea Volcano (Hawai'i) and at Gale crater (Mars). *Journal of Geophysical Research: Planets*, *125*, e2019JE006324. https://doi.org/10.1029/2019JE006324

Mozley, P. (2003). Diagenetic structures. In G. V. Middleton, M. J. Church, M. Coniglio, L. A. Hardie, & F. J. Longstaffe (Eds.), *Encyclopedia of sediments and sedimentary rocks* (pp. 219–225). Dordrecht, Netherlands: Springer. https://doi.org/10.1007/978-1-4020-3609-5_67

Mozley, P. S., & Davis, J. M. (2005). Internal structure and mode of growth of elongate calcite concretions: Evidence for small-scale, microbially induced, chemical heterogeneity in groundwater. *Geological Society of America Bulletin*, *117*(11), 1400. https://doi.org/10.1130/b25618.1

Nachon, M., Clegg, S. M., Mangold, N., Schröder, S., Kah, L. C., Dromart, G., et al. (2014). Calcium sulfate veins characterized by ChemCam/Curiosity at Gale crater, Mars. *Journal of Geophysical Research: Planets*, *119*, 1991–2016. https://doi.org/10.1002/2013JE004588

Nachon, M., Mangold, N., Forni, O., Kah, L. C., Cousin, A., Wiens, R. C., et al. (2017). Chemistry of diagenetic features analyzed by ChemCam at Pahrump Hills, Gale crater, Mars. *Icarus*, *281*, 121–136. https://doi.org/10.1016/j.icarus.2016.08.026

Piñeiro, G., Ramos, A., Goso, C., Scarabino, F., & Laurin, M. (2012). Unusual environmental conditions preserve a Permian Mesosaur-Bearing Konservat-Lagerstätte from Uruguay. *Acta Palaeontologica Polonica*, *57*(2), 299–318. https://doi.org/10.4202/app.2010.0113

Porter, E. W., & James, W. C. (1986). Influence of pressure, salinity, temperature and grain size on silica diagenesis in quartzose sandstones. *Chemical Geology*, *57*(3), 359–369. https://doi.org/10.1016/0009-2541(86)90058-6

Potter, S. L., Chan, M. A., Petersen, E. U., Dyar, M. D., & Sklute, E. (2011). Characterization of Navajo sandstone concretions: Mars comparison and criteria for distinguishing diagenetic origins. *Earth and Planetary Science Letters*, *301*(3–4), 444–456. https://doi.org/10.1016/j.epsl.2010.11.027

Putnis, A., & Mauthe, G. (2001). The effect of pore size on cementation in porous rocks. *Geofluids*, *1*(1), 37–41. https://doi.org/10.1046/j.1468-8123.2001.11001.x

Raiswell, R., & Fisher, Q. J. (2000). Mudrock-hosted carbonate concretions: A review of growth mechanisms and their influence on chemical and isotopic composition. *Journal of the Geological Society*, *157*(1), 239–251. https://doi.org/10.1144/jgs.157.1.239

Rampe, E. B., Bristow, T. F., Morris, R. V., Morrison, S. M., Achilles, C. N., Ming, D. W., et al. (2020). Mineralogy of Vera Rubin ridge from the Mars Science Laboratory CheMin Instrument. *Journal of Geophysical Research: Planets*, *125*, e2019JE006306. https://doi.org/10.1029/2019JE006306

Rapin, W., Meslin, P.-Y., Maurice, S., Vaniman, D., Nachon, M., Mangold, N., et al. (2016). Hydration state of calcium sulfates in Gale crater, Mars: Identification of bassanite veins. *Earth and Planetary Science Letters*, *452*, 197–205. https://doi.org/10.1016/j.epsl.2016.07.045

Rivera-Hernández, F. (2020a). Gini index mean score grain size estimates for Murray formation rocks (Gale crater, Mars) from ChemCam LIBS data (sols 766-1804) (Version 1) [Data set]. Zenodo. https://doi.org/10.5281/ZENODO.3605602

Rivera-Hernández, F. (2020b). Gini index mean score grain size estimates for Murray formation rocks in the Vera Rubin ridge (Gale crater, Mars) from ChemCam LIBS data (sols 1808-2298) (Version 1) [Data set]. Zenodo. https://doi.org/10.5281/ZENODO.3672073

Rivera-Hernández, F., Sumner, D. Y., Mangold, N., Banham, S. G., Edgett, K. S., Fedo, C. M., et al. (2020). Grain size variations in the Murray formation: Stratigraphic evidence for changing depositional environments in Gale crater, Mars. *Journal of Geophysical Research: Planets*, *125*, e2019JE006230. https://doi.org/10.1029/2019JE006230

Rivera-Hernández, F., Sumner, D. Y., Mangold, N., Stack, K. M., Forni, O., Newsom, H., et al. (2019). Using ChemCam LIBS data to constrain grain size in rocks on Mars: Proof of concept and application to rocks at Yellowknife Bay and Pahrump Hills, Gale crater. *Icarus*, *321*, 82–98. https://doi.org/10.1016/j.icarus.2018.10.023

Robinson, M., Collins, C., Leger, P., Kim, W., Carsten, J., Tompkins, V., et al. (2013). Test and validation of the Mars Science Laboratory Robotic Arm. In *2013 8th International Conference on System of Systems Engineering* (pp. 184–189). https://doi.org/10.1109/SYSoSE.2013.6575264

Smith, D. E., Zuber, M. T., Frey, H. V., Garvin, J. B., Head, J. W., Muhleman, D. O., et al. (2001). Mars Orbiter Laser Altimeter: Experiment summary after the first year of global mapping of Mars. *Journal of Geophysical Research*, 23689–23722. https://doi.org/10.1029/2000JE001364

Stack, K. M., Grotzinger, J. P., Kah, L. C., Schmidt, M. E., Mangold, N., Edgett, K. S., et al. (2014). Diagenetic origin of nodules in the Sheepbed member, Yellowknife Bay formation, Gale crater, Mars: Diagenetic Nodules in Gale Crater. *Journal of Geophysical Research: Planets*, *119*(7), 1637–1664. https://doi.org/10.1002/2014JE004617

Stack, K. M., Grotzinger, J. P., Lamb, M. P., Gupta, S., Rubin, D. M., Kah, L. C., et al. (2019). Evidence for plunging river plume deposits in the Pahrump Hills member of the Murray formation, Gale crater, Mars. *Sedimentology*, *66*(5), 1768–1802. https://doi.org/10.1111/sed.12558

Stein, N., Grotzinger, J. P., Schieber, J., Mangold, N., Hallet, B., Newsom, H., et al. (2018). Desiccation cracks provide evidence of lake drying on Mars, Sutton Island member, Murray formation, Gale crater. *Geology*, *46*(6), 515–518. https://doi.org/10.1130/G40005.1

Sunagawa, I. (1994). Chapter 2 Nucleation, growth and dissolution of crystals during sedimentogenesis and diagenesis. In K. H. Wolf, & G. V. Chilingarian (Eds.), Developments in sedimentology (Vol. 51, pp. 19–47). Amsterdam, Netherlands: Elsevier. https://doi.org/10.1016/S0070-4571(08)70435-7

Sun, V. Z., Stack, K. M., Kah, L. C., Thompson, L., Fischer, W., Williams, A. J., et al. (2019). Late-stage diagenetic concretions in the Murray formation, Gale crater, Mars. *Icarus*, *321*, 866–890. https://doi.org/10.1016/j.icarus.2018.12.030

Thomson, B. J., Bridges, N. T., Milliken, R., Baldridge, A., Hook, S. J., Crowley, J. K., et al. (2011). Constraints on the origin and evolution of the layered mound in Gale crater, Mars using Mars Reconnaissance Orbiter data. *Icarus*, *214*(2), 413–432. https://doi.org/10.1016/j.icarus.2011.05.002

Vaniman, D. T., Bish, D. L., Ming, D. W., Bristow, T. F., Morris, R. V., Blake, D. F., et al. (2014). Mineralogy of a Mudstone at Yellowknife Bay, Gale Crater, Mars. *Science*, *343*(6169), 1243480–1243480. https://doi.org/10.1126/science.1243480

Wang, H. L., Xu, W. Y., Cai, M., Xiang, Z. P., & Kong, Q. (2017). Gas permeability and porosity evolution of a porous sandstone under repeated loading and unloading conditions. *Rock Mechanics and Rock Engineering*, *50*(8), 2071–2083. https://doi.org/10.1007/s00603-017-1215-1

Warner, N., Silverman, M., Samuels, J., DeFlores, L., Sengstacken, A., Maki, J., et al. (2016). The Mars Science Laboratory Remote Sensing Mast. Paper presented at 2016 IEEE Aerospace Conference, Big Sky, MT USA. https://doi.org/10.1109/AERO.2016.7500554

Wentworth, C. K. (1922). A scale of grade and class terms for clastic sediments. *The Journal of Geology*, *30*(5), 377–392. https://doi.org/10.1086/622910

Wiens, R. C. (2013). MSL Mars ChemCam LIBS Spectra 4/5 RDR V1.0 [Data set].NASA Planetary Data System. https://doi.org/10.17189/1519485

Wiens, R. C., Maurice, S., Barraclough, B., Saccoccio, M., Barkley, W. C., Bell, J. F., et al. (2012). The ChemCam Instrument Suite on the Mars Science Laboratory (MSL) Rover: Body Unit and combined system tests. *Space Science Reviews*, *170*(1), 167–227. https://doi.org/10.1007/s11214-012-9902-4

Wiens, R. C., Maurice, S., Lasue, J., Forni, O., Anderson, R. B., Clegg, S., et al. (2013). Pre-flight calibration and initial data processing for the ChemCam laser-induced breakdown spectroscopy instrument on the Mars Science Laboratory rover. *Spectrochimica Acta Part B: Atomic Spectroscopy*, *82*, 1–27. https://doi.org/10.1016/j.sab.2013.02.003

Yingst, R. A., Bray, S., Herkenhoff, K., Lemmon, M., MinittiSchmidt, M. E. M. E., Schmidt, M. E., et al. (2020). Dust cover on Curiosity's Mars Hand Lens Imager (MAHLI) calibration target: Implications for deposition and removal mechanisms. *Icarus*, *351*, 113872. https://doi.org/10.1016/j.icarus.2020.113872

Yoshida, H., Hasegawa, H., Katsuta, N., Maruyama, I., Sirono, S., Minami, M., et al. (2018). Fe-oxide concretions formed by interacting carbonate and acidic waters on Earth and Mars. *Science Advances*, *4*(12), eaau0872. https://doi.org/10.1126/sciadv.aau0872